UNIVERSITY OF CALIFORNIA SAN DIEGO

Zirconium-Oxo Cluster-Functionalized Silica Nanoparticles for Removal of Toxic Chemicals

A Thesis submitted in partial satisfaction of the requirements

for the degree Master of Science

in

Chemistry

by

Yubin Huang

Committee in charge:

Professor Michael Sailor, Chair
Professor Joshua Figueroa
Professor Andrea Tao

2022

The Thesis of Yubin Huang is approved, and it is acceptable in quality and form for publication on microfilm and electronically.

University of California San Diego

2022

TABLE OF CONTENTS

LIST OF FIGURES

LIST OF TABLES

ACKNOWLEDGEMENTS

Undertaking this Master's degree at UCSD has been a truly life-changing experience for me and it would not be possible to do without the support and guidance that I received from many people.

I would like to express my deepest appreciation to my supervisors Prof. Michael Sailor and Prof. Joshua Figueroa for countless support and encouragement they gave me. Their guidance helped me in the time of research and putting up this work. This project would not have been possible without them.

I would like to acknowledge the Defense Advanced Research Projects Agency (DARPA) and Naval Information Warfare Center Pacific, (NIWC Pacific) for their funding support (contract No. N66001-21-C-4010). Thanks should also go to the UC San Diego Materials Research Science and Engineering Center (UCSD MRSEC, DMR-2011924) for granting access to the instruments.

I would like to extend my sincere thanks to Yi-sheng Lu, PhD and Vincent Wang, PhD, who served as my mentors and challenged me to become a better qualified researcher. Thanks should also go to Ricardo De Luna, who took care of the laboratory matters and provided trainings to the instruments. Additionally, this endeavor would not have been possible without the generous support from the members of the Sailor lab, who impacted and inspired me.

Lastly, I would be remiss not mentioning to my family, especially my parents and my girlfriend. Their belief in me has kept me spirits and motivation high during this process.

The full chapters are currently being prepared for submission for publication of the material. Yubin Huang, the thesis author, was the primary investigator and author of this material. Vincent Wang synthesized the catalyst. Yi-sheng Lu and Vincent Wang provided research directions and edited this manuscript in full.

ABSTRACT OF THE THESIS

Zirconium-Oxo Cluster-Functionalized Silica Nanoparticles

for Removal of Toxic Chemicals

by

Yubin Huang

Master of Science in Chemistry

University of California San Diego, 2022

Professor Michael Sailor, Chair

The efficient adsorption or catalytic degradation of toxic chemicals is desired to provide effective personal protection in both industrial and possible military situations. The possibility of both chemical warfare agents (CWAs, *e.g.*, VX) and toxic industrial chemicals (TICs, *e.g.*, NH_3)

being released underscores the need for new materials capable of sequestering and/or decontaminating these chemicals. For this purpose, we developed a new composite material by conjugating an inorganic molecule with nano-sized silica support. Specifically, zirconium (oxo) hydroxy methacrylate (Zr cluster) composed of a $Zr_6O_4(OH)_4$ node and methacrylate backbones is polymerized on the surface of silica (SiO_2) nanoparticles upon UV irradiation, and this composite material is tested for (1) catalytic hydrolysis of a CWA simulant, dimethyl p-nitrophenyl phosphate (DMNP) and (2) adsorption of a TIC, ammonia. The composite material displays superior catalytic performance towards DMNP hydrolysis compared to the "free" Zr cluster, and it also shows greater adsorption capacity for NH_3 than the bare silica nanoparticles. The advantage of the low-cost and low-complexity of the synthesis is demonstrated in a notional clothing decontamination scenario, where the Zr-silica composite catalyst is embedded in fabric swatches and evaluated for its adsorption and decontamination capabilities.

1. ZIRCONIUM OXO HYDROXY METHACRYLATE (ZR CLUSTER)

1.1. SYNTHESIS OF THE CLUSTER

The crystalline zirconium (oxo) hydroxy methacrylate (Zr cluster) was synthesized by reaction of metal alkoxide in the presence of excess carboxylic acid in an alcoholic solution following a previous reported procedure.[1] Briefly, 1 mL of 70% zirconium (IV) propoxide solution in 1-propanol was added in a dried Schlenk tube under N_2 with 1.5 mL of methacrylic acid. The closed vessel was stored at room temperature and shielded from ambient light. A precipitate of the clear crystalline solid was observed after one day. The cluster was purified by rinsing with dichloromethane, then pentane to remove the excess methacrylic acid. Approximately 700 mg of the Zr cluster was collected.

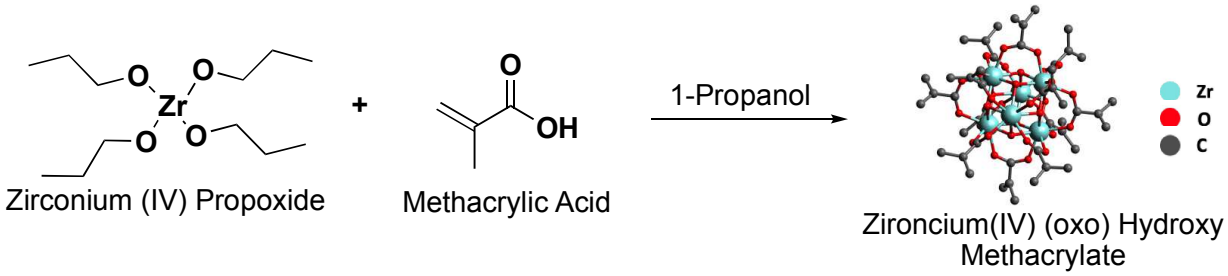

Figure 1-1 Schematic drawing of Zr cluster preparation.

Prior work has shown that the in-situ production of water resulting from the esterification of propanol and methacrylic acid induces partial hydrolysis of the zirconium alkoxide. The high oxidation state of the hydrolyzed Zr^{IV} cation is expected to display a strong Lewis acidity, in which the presence of minor amounts of water results in hydrolysis of the metallic Zr^{IV} cation to form stable metal-oxygen bonds. Upon self-assembly, the oxide oxo core $Zr_6O_4(OH)_4$ is bridged by alternating μ_3-O and μ_3-OH groups, and the coordination vacancy was stabilized by 12 methacrylic

acids, among which of the capping ligands, three carboxylate ligands chelate the zirconium atom at one μ_3-O capped face, while the other nine carboxylate ligands bridge all edges of the Zr_6 octahedron except the edges of the chelated face.[2-4]

Researchers have used the versatile vinyl backbones on the Zr oxo cluster for broadly useful Zr-based organic-inorganic copolymers[5-8], and substitution of the labile bridging-chelating backbones can be useful for synthesis of metal organic frameworks (MOF)[9, 10]. The simplicity and low cost of the synthetic process of Zr oxo cluster are of interest for applications as in the integrated optics devices,[11] the extreme-ultraviolet photoresists in lithography,[12] and encapsulant for light-emitting diode[13].

More importantly, investigations of the ligand exchange dynamic of the $Zr_6O_4(OH)_4$ cluster core have demonstrated the electrophilic cluster core is dynamically stabilized by labile ligands, and OH ions and water molecules take the place of the bidentate ligand [3, 14], giving it an anticipating prospect as a Lewis acidic catalyst, where the metal oxide core with a vacant coordination site (a defect) then becomes the catalytic active site available for coordination with Lewis basic compounds.[15, 16]

1.2. PHYSICAL CHARACTERIZATION

The presence of the MA ligands appended to the zirconium node was confirmed by the attenuated total reflectance Fourier-transform infrared (ATR-FTIR) spectra (Figure 2.2). The major peaks are as follows: C=O stretching vibration of carboxyl group (1688 cm^{-1}); C=C stretching vibration of methacrylate (1633 cm^{-1}); stretching vibration of carboxyl group bound to Zr cores (ν_{AS}, 1573 or 1546 cm^{-1}; ν_S 1440, 1411, and 1370 cm^{-1}); (ν (CMeCH2), 1243 cm^{-1}); the wagging vibration of methacrylate (997 and 931 cm^{-1}); the bending vibration of Zr-O-Zr (655 cm^{-1}).[12]

Further characterization of the Zr cluster was assessed by thermogravimetric analysis (TGA) shown in Figure 2.2. The TGA data suggests the thermal stability of the Zr_6-cluster can be tolerated up to 400˚C without obvious degradation. The weight loss begins from 400˚C is associated with the vaporization of the chelating-bridging MA ligands,[13] and the remaining mass is due to the monolithic zirconium dioxide/hydroxide[12], which has a melting point of 2715˚C [17], beyond the temperature range applied here. An average weight loss of 57.0% is highly correlated with the theoretical value (56.5%) calculated based on the mass percentage of the organic ligands in the cluster.

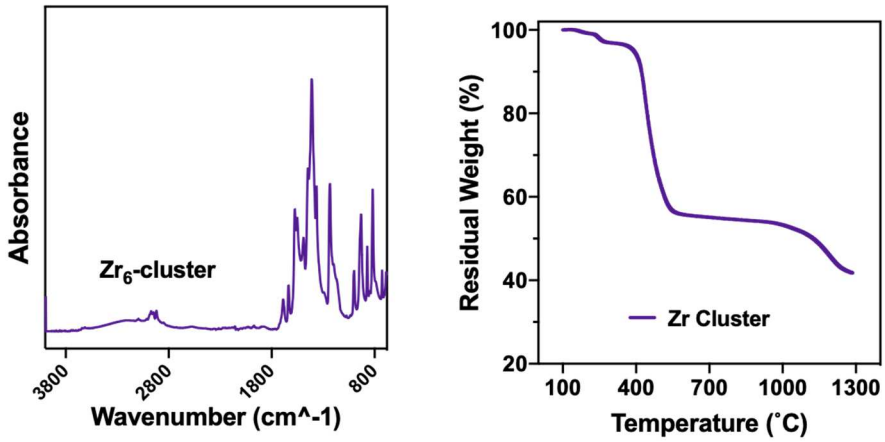

Figure 1-2 FTIR spectrum of Zr cluster (left) TGA plot of Zr cluster (right).

2. ZIRCONIUM CLUSTER LOADED ON SILICA FOR ENHANCED HYDROLYSIS OF CHEMICAL AGENT

2.1. DETOXIFYING CHEMICAL NERVE AGENTS

Detoxifying chemical warfare agents (CWAs) is of primary concern for homeland defense due to their acute toxicity. There are five major categories of CWAs: choking agents, blister agents, blood agents, nerve agents, and riot control agents. Among these, nerve agents (NAs) are regarded as the most fatal with rapid effects because they are capable of deactivating an enzyme called acetylcholinesterase (AchE) in the nervous system, and the inhibition of this enzyme often leads to muscle paralysis or causes death in higher doses (Figure 1-1). Trace amounts can lead to paralysis and high doses can cause painful death, typically by asphyxiation.[18] Discovery of the bioactivity against organism led to the initial deployment of OP agents as insecticides for agriculture purposes and domestic applications in the early 20th century. However, these chemical compounds were far too toxic to be used solely for killing the insects and soon they were largely manufactured for CWAs (e.g., GA, GB, GD, and VX shown in Figure 1-1) that had deployed during World War I and caused death on a vast scale.[19]

With the international effort of banning the use of these agents, 193 members states have committed upon the prohibition of the development, production, stockpile, and use of chemical weapons according to the Organization of Prohibition Chemical Weapons (OPCW). Technologies to eliminate stockpiled CWA, converting to a form unsuitable for production of chemical weapons can be classified into two: (1) high temperature destruction technologies including plasma pyrolysis, incineration, and explosion chambers, and (2) low temperature destruction technologies

including hydrolysis, which involves a process using a strong basic solution (e.g. NaOH) to render corresponding phosphonic acid.

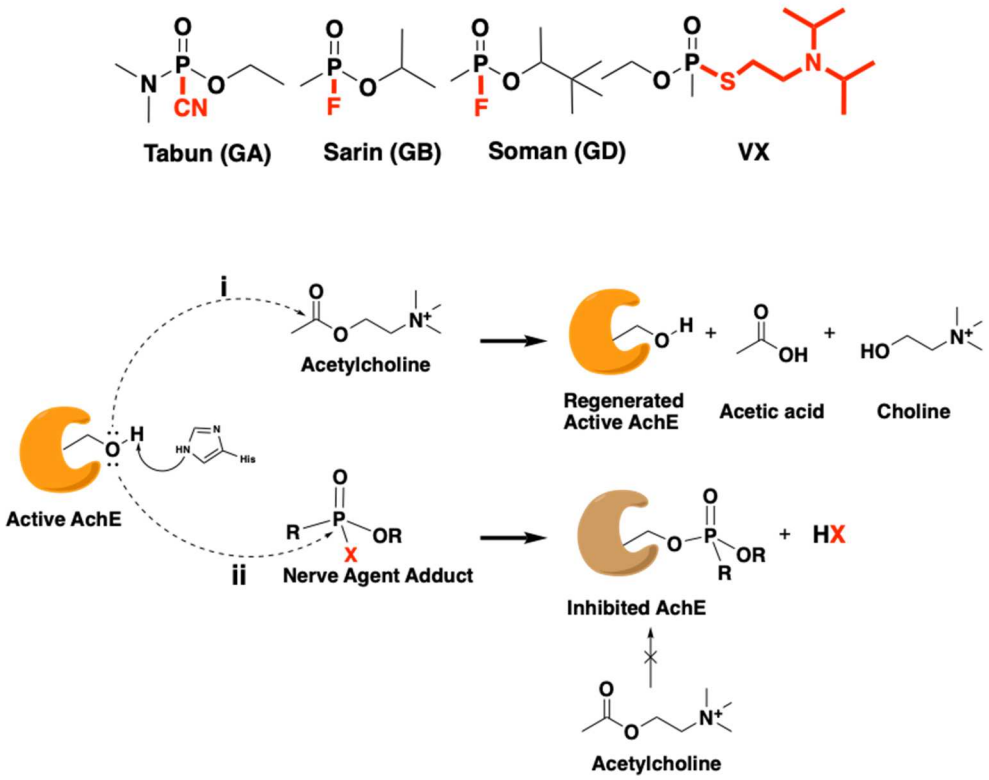

Figure 2-1 Examples of CWAs with the leaving groups lighted in red (top); AchE inhibition pathway (bottom).

However, the necessary for specific reaction chambers or large excess caustic solution have limited the feasibility of these destruction technologies for personal use against airborne chemical toxin. Recently, personal protective wearables integrated with particulates possessing high porosity and surface area have received a broad interest.[20] One example is the use of activated carbon that enables capturing and removal of NAs via physical adsorption, which is mostly used in gas mask filters for commercial, industrial, and military applications. ASZM-TEDA, a high surface area composite of porous activated carbon adsorbent, impregnated with triethylenediamine

(TEDA) and compounds of metal oxides, including Cu ('A'), Ag ('S'), Zn ('Z'), and Mo ('M').[21] However, the limited capability in detoxifying the agents is of critically challenging for safe disposal of the contaminated materials afterward. A broad scope of materials, such as polymers,[22-24] functionalized nanoparticles,[25, 26] and MOFs[27-33] have been developed for decomposition of NAs through catalytic hydrolysis. Among the broad-spectrum protection against OP, metal oxides-based materials are known to outperform others because the strong Lewis's acidity of the metal defected site is capable of activating OP species, resulting a rapid nucleophilic attack with a hydroxyl group.

In this regard, we developed Zr cluster based-nanotechnological subsystem that can be incorporated into a fabric as a component of an outer garment that will prevent agent contact by the wearer. The subsystem has been engineered to enhanced catalytic rate for hydrolysis of OP.

2.2. SYNTHESIS OF NONPOROUS SILICA

Silica is by far the most abundant component of the Earth's crust, most often found as crystalline quartz composed of SiO_4 tetrahedra organized into periodic structure. The silica particles extracted from nature resources contain impurities which are not favorable for scientific research and industrial applications. Therefore, focus has been given to synthetic silica, usually amorphous, as opposed to the crystalline silica, because the controlled synthetic can be useful for producing pure silica particles and providing morphology control through systematic monitoring of reaction parameters. There are two distinguish synthetic pathways to prepare silica nanoparticles (NPs)[34]: (1) fumed silica synthesized via flame pyrolysis of $SiCl_4$ with hydrogen at high temperature (1200-1400˚C) and (2) colloidal silica synthesized via reversible hydrolysis and condensation (so-called sol-gel) reactions in liquid medium.

Colloidal silica NPs are stable dispersions of discrete particles in a liquid medium, unliked fumed silica often displayed as string-of-pearl like morphology and mostly aggregated particles.[34] The sol-gel process is widely applied to produce colloidal nanoparticles due to its ability to produce particles with homogeneous size distributions at mild conditions. Colloidal silica NPs used in this study were prepared by the Stöber process[35] following a previously reported procedure[36]. There are three advantages of using this material: (1) this base-catalyzed (pH 7-10) sol-gel method has been demonstrated to generate monodispersed silica NPs with high yield and great stability, (2) silica particles are known for their versatile silanol groups on the surface for conjugation of small molecules, and catalyst located on the external surface avoids the hindrance of substrate diffusion.

A typical synthesis of SiO_2 nanoparticles is as follow[36], to a 250 mL round bottom flask, 115 mL ethanol, 8 mL 25% ammonia, and 3 mL diH_2O were stirred at 60˚C. 6 mL of TEOS was slowly added to the solution in 1 minutes and stirred overnight at 60˚C. The silica NPs were collected by centrifuge (11000 rpm, 10 mins) and redisperse-centrifuge in ethanol solution for three cycles and then dried in a tube furnace at 120˚C for 2 hours. Approximately 1.2 g of SiO_2 can be collected.

The silica synthesis involves a catalyzed hydrolysis of tetraethyl orthosilicate (TEOS) in an alkaline condition. This solution of this step generally contains saturated silicic acid, $Si(OH)_4$. A reversible polycondensation between the two silanol groups (≡Si-OH) forms the siloxane bridging (≡Si-O-Si≡) within the particles and leaves the unreacted hydroxyl groups on the particle surface as shown in Figure 3.1. Gao and etc reported a facile way to the control the size of silica NP from 73 nm to 398 nm through adjusting the volume of ethanol.[36] They reported the size of the silica NP is inverse proportion to the ethanol volume used in the sol-gel reaction. Calcination treatment after the synthetic process usually reduces the density of surface hydroxyl groups and

generates a hydrophobic surface of the NPs through dehydration condensation reaction.[37] To rehydrate the surface of silica, the way to make the surface becoming hydrophilic is to hydrolyzes the ≡Si–O–Si ≡ bridging on the surface with water to replenish surface hydroxyl groups, which can aid the dispersity of the NPs in aqueous or organic mediums and be useful for downstream surface modifications.

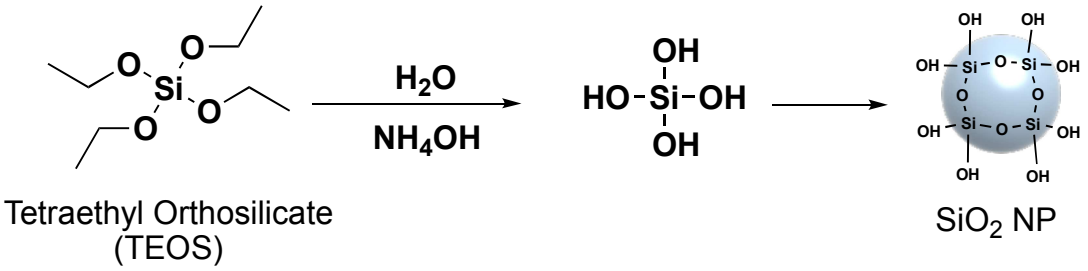

Figure 2-2 One step synthesis of SiO_2 NP in the presence of ammonia as catalyst. Two main reactions include hydrolysis of TEOS and polycondensation of $Si(OH)_4$.

2.3. CHARACTERIZATION OF SILICA NANOPARTICLES

To exam the uniformity of the synthesized silica NP, Dynamic Light Scattering (DLS) measurement was first used to measure the as-prepared silica NPs displayed an average particle size of 128.2 ± 0.3 nm with a poly-dispersive index (PDI) of 0.017 (Figure 2-3). The silica NPs show a negative zeta potential of -35.9 ± 0.7 mV due to the deprotonation of the surface hydroxyl groups (Figure 2-3).[34] The mono-dispersity of the as-prepared silica NPs is shown in the scanning electron microscope (SEM) images in Figure 2-4 (a). FTIR displays a strong band at 1030 cm^{-1} associated with Si-O stretching modes of the SiO_2, and the stretching and bending modes at 3320 cm^{-1} and 1660 cm^{-1} assigned to a combination of surface O-H and adsorbed water (Figure 2-5).[38, 39] The TGA reveals a weight loss of 5.6 ± 0.2%, which can be attributed to the removal of the

surface hydroxyl groups (Figure 2-8 a). Nitrogen adsorption/desorption isotherms (Figure 2-7) shows a specific surface area of 34.7 ± 2.7 m^2/g for the nonporous silica NPs using BET (Brunnauer-Emmett-Teller) analysis.

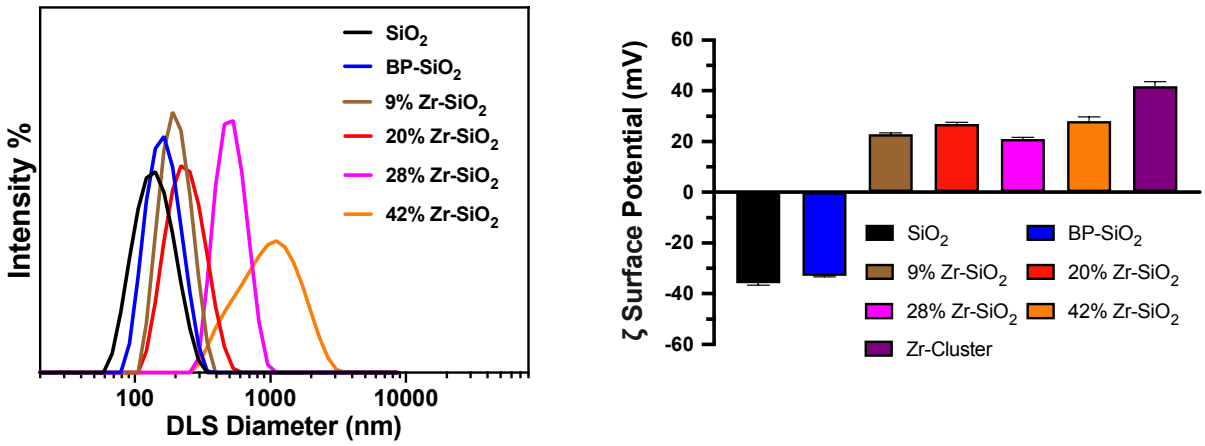

Figure 2-3 DLS diameter and particles zeta surface potential for SiO_2 NPs and surface modified SiO_2 NPs.

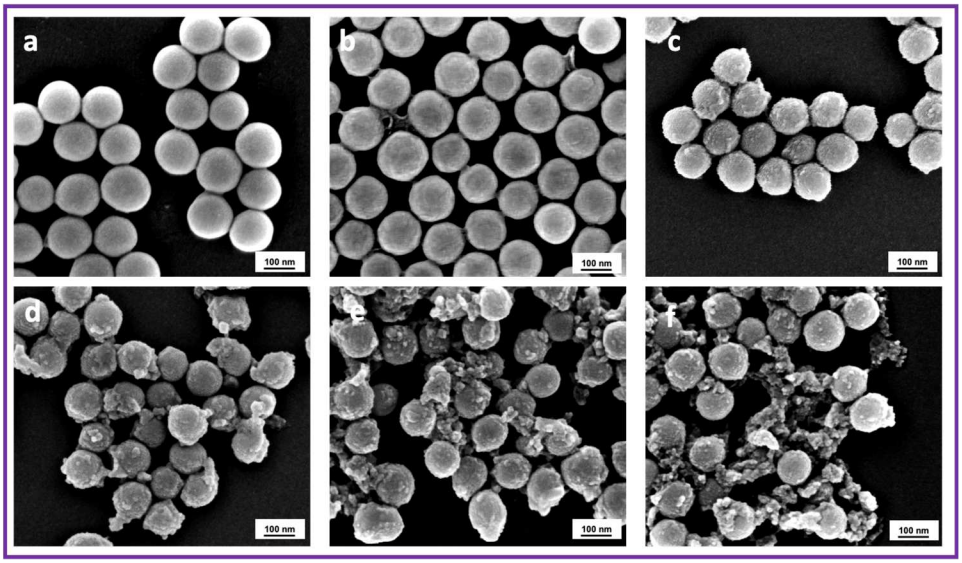

Figure 2-4 SEM images SiO_2 NP (a) SiO_2, (b) BP-SiO_2, (c) Zr-SiO_2 (9%), (d) Zr-SiO_2 (20%), (e) Zr-SiO_2 (28%), and (f) Zr-SiO_2 (42%).

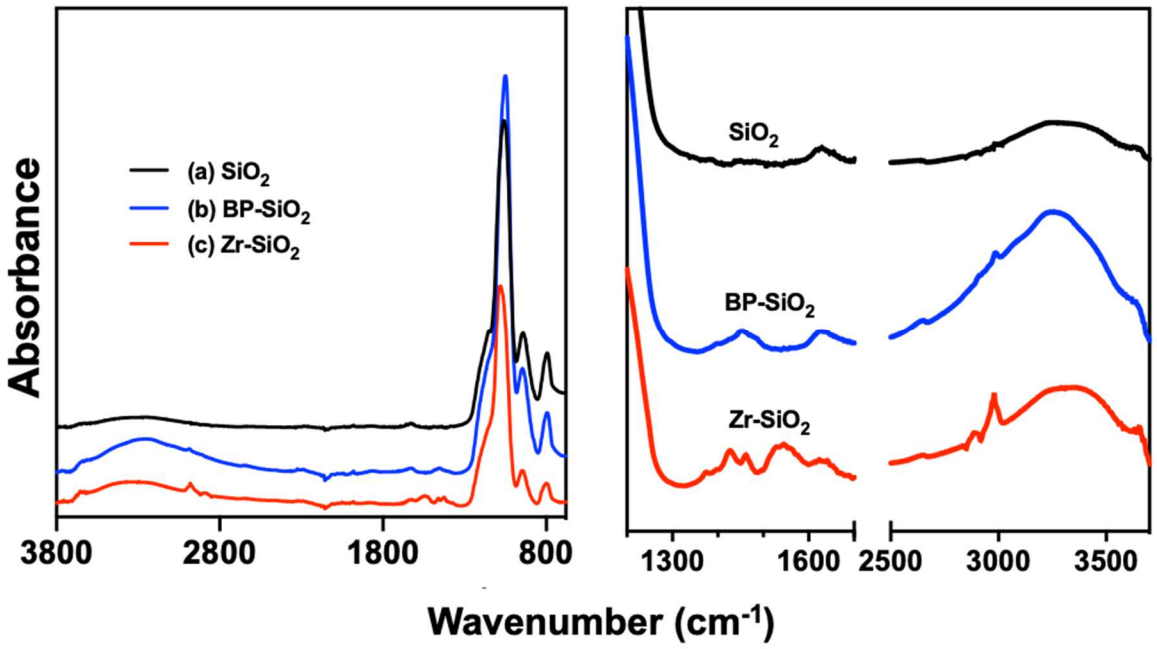

Figure 2-5 FTIR spectrums for SiO_2, BP-SiO_2 and Zr-SiO_2. Zoomed in spectrum is on the right.

2.4. GRAFTING OF ZR CLUSTERS ON SILICA NANOPARTICLES

In a typical experiment of Zr cluster sequential grafting on silica NPs (20% Zr-SiO_2), 200 mg of silica NPs was first sonicated in 20 mL of water overnight to rehydrate the surface. After the removal of the solution by centrifugation (10,000 rpm, 10 mins), the silica NPs and 50 mg of benzophenone (BP) were dispersed in 30 mL of tetrahydrofuran (THF) in a 50 mL round bottom flask. The container was subjected to nitrogen gas for 30 minutes to remove oxygen (polymerization inhibitor) prior to the UV irradiation. A high-pressure mercury lamp with broad wavelength was set to irradiate the sample for 20 mins with stirring. Excess of the free BP was then removed and washed in THF solution. In the 20% mass loading condition, 60 mg of the Zr_6-clusters was added to the BP-SiO_2 NPs and suspended in 30 mL of THF solution. The mixture was bubbled with nitrogen for 30 mins, then UV irradiated for 1 hour. The Zr-SiO_2 NPs were collected by centrifugation and washed with THF to remove unbonded Zr_6-cluster. The Zr-SiO_2 NPs were

dried in a vacuumed oven at 80˚C for 2 hours to remove residual organic solvent prior to physical characterization.

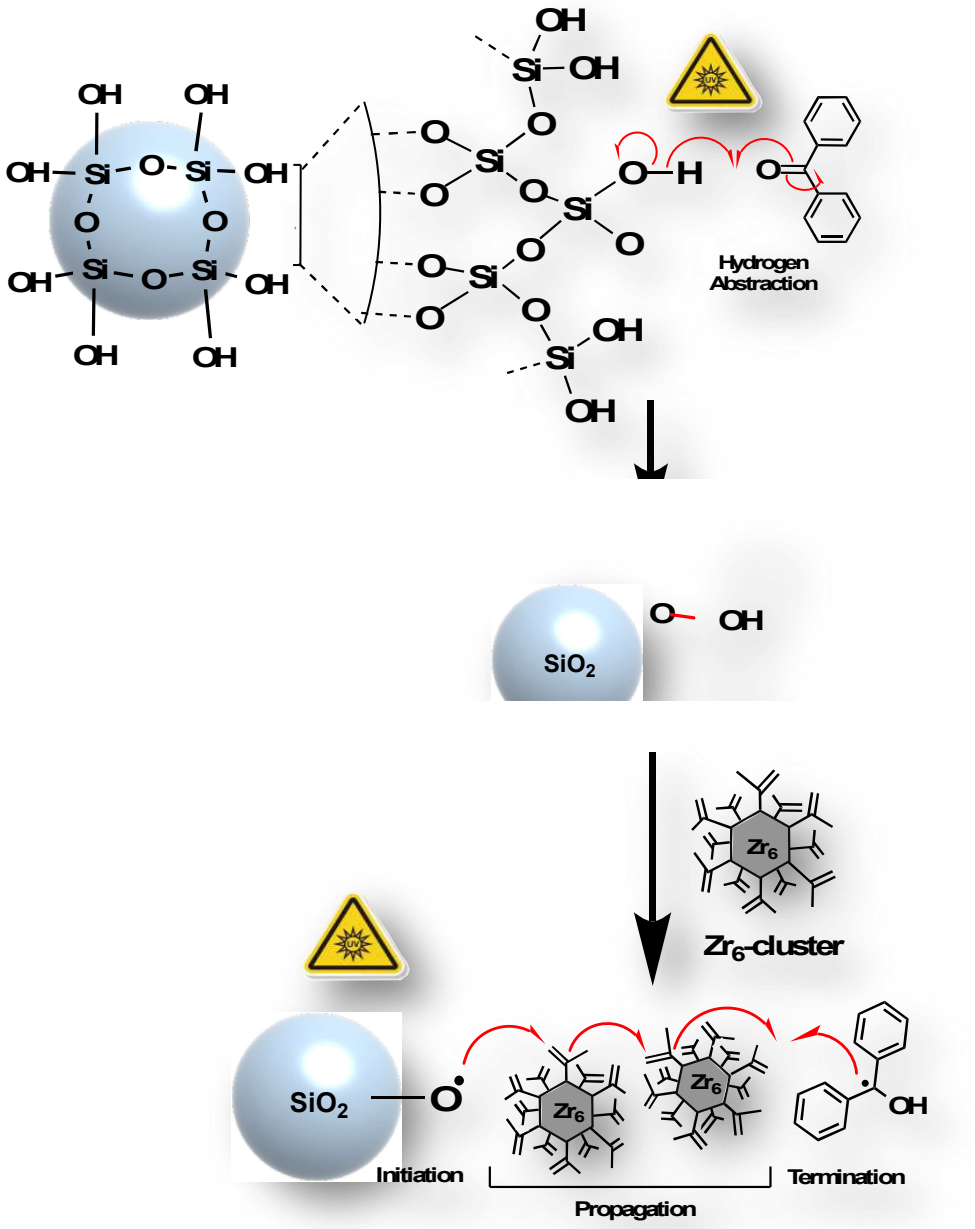

Figure 2-6 Schematic drawing of UV-induced grafting of Zr cluster on silica surface in the presence of photoinitiator benzophenone.

To explore a facile method for immobilizing the Zr_6-cluster, we initially adopted a "one-pot" method. The NPs were introduced to a THF solution of Zr_6-cluster, and the mixture was irradiated in the presence of a Type II photoinitiator benzophenone (BP). However, the excess non-NP-bonded BP causes severe self-aggregation of the Zr_6-cluster, significantly hampering the grafting (data not shown here). A sequential (2-steps) grafting method was then adopted, and the mechanism is shown in Figure 2-6. It began with hydrogen abstraction of the hydroxyl group on the silica NP surfaces upon irradiation in the presence of BP to afford the activated initiating species, $\equiv SiO–C(OH)(Ph)_2$, namely BP-SiO_2. After removing the unreacted BP by centrifuge, a solution of Zr_6-cluster in THF was subsequently introduced to the BP-SiO_2 NPs. Further irradiation was required for MAs of the Zr_6-cluster to propagate and form highly branched polymers on the NP surface via radical mechanism. This 2-steps method shows significant improvement on the loading yielding in comparison to the "one-pot" method due to the elimination of the ligands induced radical species.[40]

The DLS measurement shows no significant increase of the BP-SiO_2 in particle sizes, and the zeta potential remains negatively charged (Figure 2-3). The SEM images (Figure 2-4) shows that the surface morphology and mono-dispersity of the BP-SiO_2 NPs remained the same as that of the bare silica NPs. The nitrogen adsorption/desorption isotherm of BP-SiO_2 (Figure 2-7) indicates that the specific surface area remained unchanged compared to the bare SiO_2 (35.5 ± 0.8 m^2/g BP-SiO_2; 34.7 ± 2.7 m^2/g SiO_2). In the FTIR spectrum (Figure 2-5), the characteristic peaks of the aromatic rings in the diphenylmethanol are observed on the silica NPs indicating the successful grafting of the photoinitiator; the new peaks for the BP-SiO_2 at 3020 cm^{-1} and 1484 cm^{-1} are attributed to the C-H and C=C stretch of the aromatic compound.[38] The TGA data (Figure 2-8) shows an additional weight loss of 1% after surface activation, suggesting the vaporization of

the surface-grafted BP. These results indicate that the BP was chemically bound to the silica substrate upon UV irradiation.

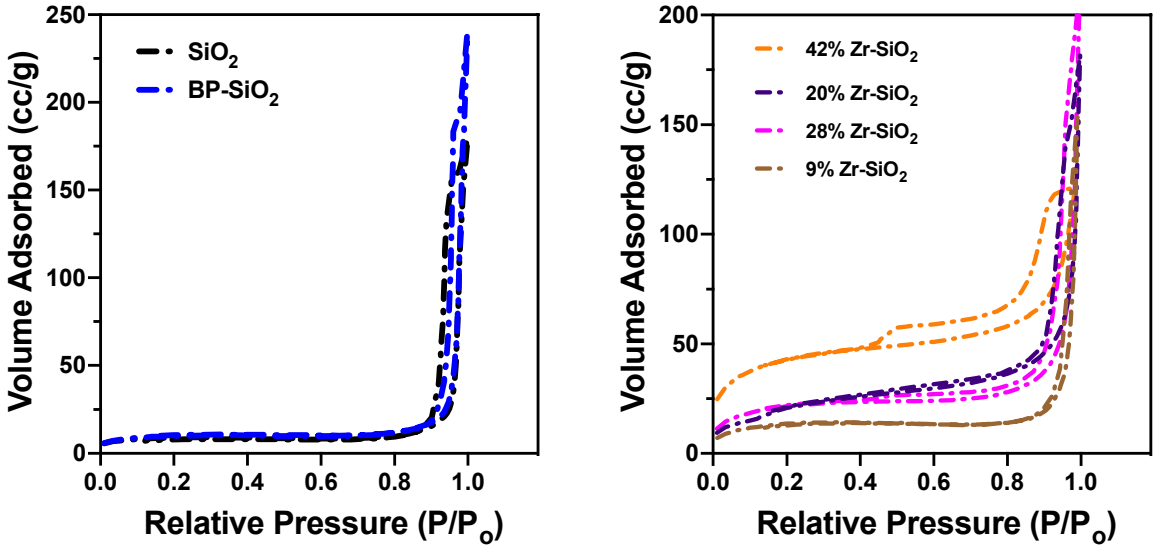

Figure 2-7 Nitrogen adsorption desorption isotherms for Zr cluster grafted SiO2 NPs.

To prove that no homopolymerized Zr_6-clusters was presented in the final composited material, Zr_6-cluster and BP were subjected to UV irradiation in the absence of silica NPs. No precipitation was able to be collected in the solvent upon centrifugation, suggesting a highly soluble nature of the polymeric Zr_6-cluster. The controlled mass loading of the Zr_6-clusters on the silica NPs was achieved by varying the concentration of the Zr_6-clusters in the solvent with standardized UV intensity, irradiation time, and the BP-SiO_2 concentration. The calculation for determining the mass loading (w/w) was defined in eq 1, where the values of the weight change percentage (WC%) are derived from the TGA curves from 100˚C to 1300˚C.

$$\text{(eq 1). Mass Loading}_{\text{TGA}}\ (\%) = \frac{\text{WC\%}_{\text{Zr-SiO}_2} - \text{WC\%}_{\text{BP-SiO}_2}}{\text{WC\%}_{\text{Zr}_6\text{-cluster}}} \times 100$$

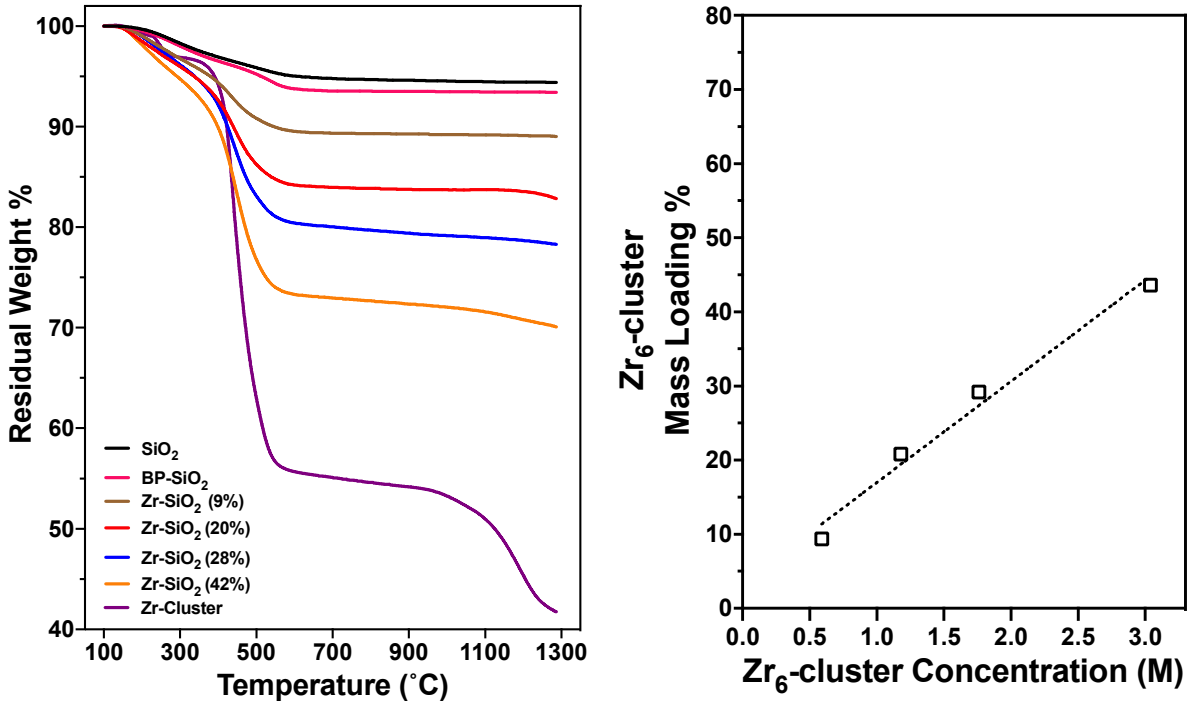

Figure 2-8 TGA plots for Zr grafted SiO2 NPs (left) and grafting efficiency with varied concentration of Zr cluster that is added for polymerization.

The tunable loading capacity of the composites was confirmed by TGA analysis (Figure 3.6), where the Zr-SiO_2 sample shows a steep weight loss from 200˚C attributed to the thermal decomposition of the BP and the MA ligands. To reach 9% to 42% (w/w) mass loading of the Zr clusters, a linear increase with respect to the Zr cluster used for the polymerization was observed (Figure 2-8). This dependence of the cluster concentrations to the mass loading confirmed that the grafting mechanism was mainly via polymerization rather than electrostatic adsorption because the mass loading for the latter case would commonly remain flat as the concentration of the payload was increased.[41, 42] The surface charge of the Zr-SiO_2 NPs (Figure 2-3) became positive as opposed to their predecessors, further supporting the appearance of the Zr_6-clusters on the silica NPs. SEM images (Figure 2-4) indicate the sequential grafting polymerization of the Zr_6 clusters occurred on

the surface, and the stacking of the NPs is pronounced for the higher loading conditions (28% and 42% Zr-SiO_2), likely caused by the polymeric crosslinking and stacking from the loaded Zr-SiO2 clusters..[43] The DLS (Figure 2-3) results show the average size of particles post grafting becoming 202, 217, 575, and 861 nm for the 9%, 20%, 28%, and 42% Zr_6-cluster mass loading conditions, respectively. The overall trend observed in DLS size distribution matched with the particle aggregation observed in SEM images. Polymerization of the Zr clusters on the NPs' surface raised the specific surface area as indicated by nitrogen adsorption/desorption isothermal measurements (Figure 2-7). Increased BET surface areas (Table 1-1), as well as the unprecedented hysteresis loop for the 42% condition suggest that such polymerization generates localized microporous morphology on the silica surface. Peaks appeared in the FTIR (Figure 2-5) can be identified to be the presence of the Zr_6-clusters on the NPs. The new peaks at 1461 cm^{-1} to 1564 cm^{-1} are attributed to the asymmetric and symmetric stretching mode of the COO^-, and the stretching mode of the C-H for the methyl and olefinic group are present at 2911 cm^{-1} and 2985 cm^{-1}.

Table 1-1. Summary of Physical Characterizations.

	Weight Loss (%)	Surface Area (m^2/g)	DLS Size (nm)	Surface Potential (mV)
SiO_2	5.6 ± 0.2	34.7 ± 2.7	128 ± 1	-35.9 ± 0.7
BP-SiO_2	6.3 ± 0.3	35.5 ± 0.8	160 ± 3	-33.0 ± 0.3
Zr_6-cluster	57.0 ± 1.0	–	–	41.8 ± 1.7
Zr-SiO_2 (9%)	10.4 ± 0.4	46.6 ± 2.8	202 ± 3	22.9 ± 0.6
Zr-SiO_2 (20%)	17.6 ± 0.2	63.1 ± 1.9	217 ± 5	26.8 ± 0.8
Zr-SiO_2 (28%)	22.2 ± 0.4	76.1 ± 0.8	575 ± 17	21.0 ± 0.7
Zr-SiO_2 (42%)	30.0 ± 0.4	152.9 ± 0.7	861 ± 16	28.0 ± 1.6

2.5. HYDROLYSIS OF DMNP IN BUFFER SOLUTIONS

A normalized concentration of the Zr_6-clusters (2.35 mM, 9.4 mol % ratio to 25 mM DMNP) in NEM buffer was used to assess the catalytic activity across the different mass loading conditions. Half-lifes ($t_{1/2}$) of the hydrolysis reactions of 25 mM DMNP were reported in Table 2. A 9 to 47-fold $t_{1/2}$ reduction were achieved upon grafting the cluster on silica NPs (Figure 2-9). Controlling reaction of BP-SiO_2 NPs in the buffer solution shows negligible conversion of the DMNP under the same protocol. The cemented evidence indicates the substantial improvements of the cluster upon loaded to the NPs. The 9% mass loaded composite gives a $t_{1/2}$ of 11.2 mins. This is owing to insufficient grafting causes the chemisorption of DMNP to the excess exposed SiO_2 on the NPs surface leading to slow kinetics of the substrate diffusion toward the loaded clusters. Hampered catalytic reactivities of overloaded materials (28% and 42%) are presumably attributed to the aggregation effect from the localized vigorous polymerization of the Zr_6-clusters, causing the substrate to be inaccessible to the shielded clusters, which was evidenced in the SEM images (Figure 2-4) and hydrodynamic size measurement (Figure 2-3). Hence, an optimized composite with 20% Zr cluster loading was synthesized and demonstrated 27-folds enhancement of the turnover frequency relative to the free Zr_6-cluster, and 3.4-folds and 1.5-folds enhancement relative to the UiO-66[28] and NU-1000[29] (Zr-MOFs) which are well-known for their reactivity towards DMNP hydrolysis.

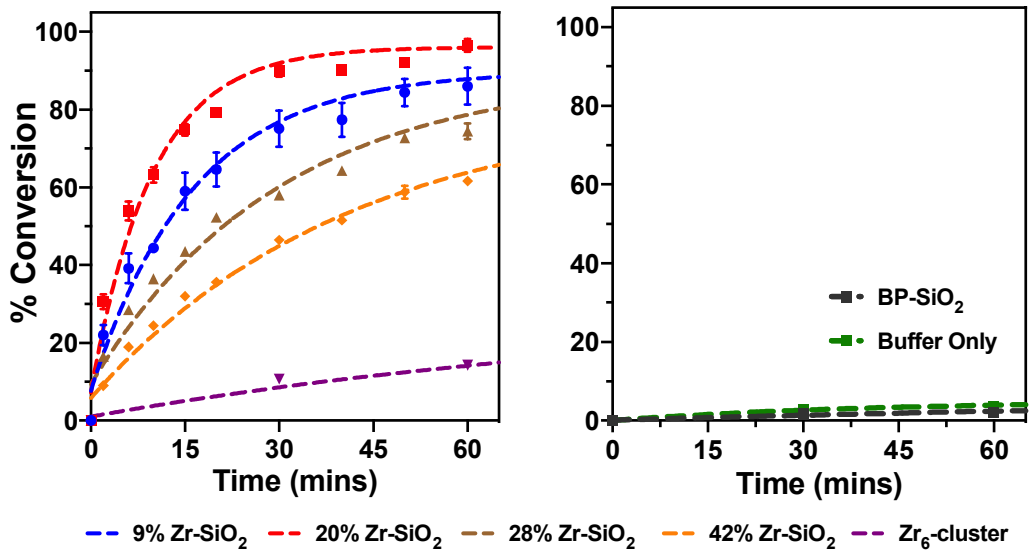

Figure 2-9 Hydrolysis of 25 mM DMNP using 9.4 mol% of catalyst in 0.4 M NEM buffer

HEPES buffer (0.1M, pH=7.4, adjusted by NaOH) has been previously reported for its utility in hydolyzing NA simulants.[32, 33] The results (Figure 2-10) showed a $t_{1/2}$ of 18 mins, and 90.3% conversion after 90 mins using the 20% Zr-SiO_2. The kinetic rate of the catalyst is dependent to the pH of the solution and surrounding proximal basic/nucleophilic sites.[27] The inferior performance of the Zr-SiO_2 at pH 7.4 buffer (18 mins, vs 6.5 mins in pH 10 NEM buffer) was likely due to the slow displacement of the coordinated hydrolysis product (dimethyl phosphate, DMP) to the Zr^{IV} site due to the lower presence of a base.

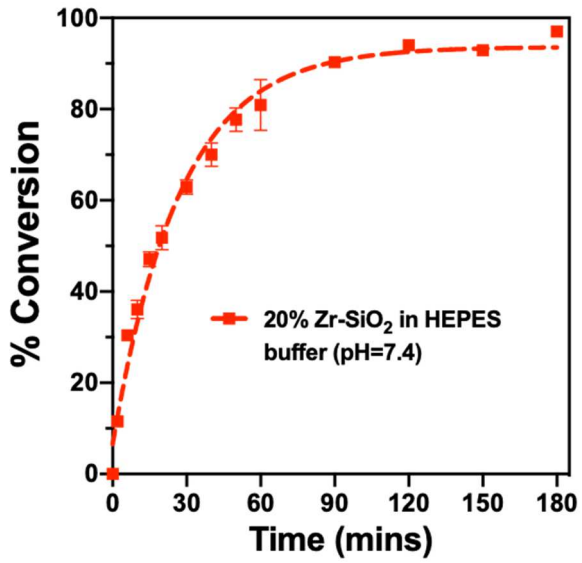

Figure 2-10 Hydrolysis of DMNP with 20% Zr-SiO_2 in HEPES pH 7.4.

To gain insight of the kinetic parameters of the Zr-SiO_2, the Michaelis-Menten (MM) model is used for comparing the activities among different mass loading of the Zr_6-cluster on SiO_2.[44, 45] The initial rates of the product formation against increasing concentrations of DMNP were plotted in Figure 2-11. Table 2 summarizes the kinetic parameters derived by the MM model. Both grafted and ungrafted Zr_6-cluster exhibited a hyperbolic dependence of the initial rate on the concentration of DMNP, and a strong linear correlation (R^2=0.996, 20% Zr-SiO_2) between the initial rates up to 25 mM DMNP suggests not all of the catalytic active sites have been saturated by DMNP; therefore, the kinetic parameters when active sites are fully saturated by substrates can hardly be obtained from the conversion profile of 25 mM DMNP. The mass loading of 20% possessed the k_{cat} and K_{cat}/K_m values of 2.36×10^{-2} s^{-1} and 0.63 $M^{-1}s^{-1}$, respectively, which is the highest among all the grafted NPs. The k_{cat} or K_{cat}/K_m values for the ungrafted Zr_6-cluster is approximately 11-folds and 16-folds lower than those of the corresponding NPs, confirming the benefits of immobilizing the catalyst on the nano-sized solid support.

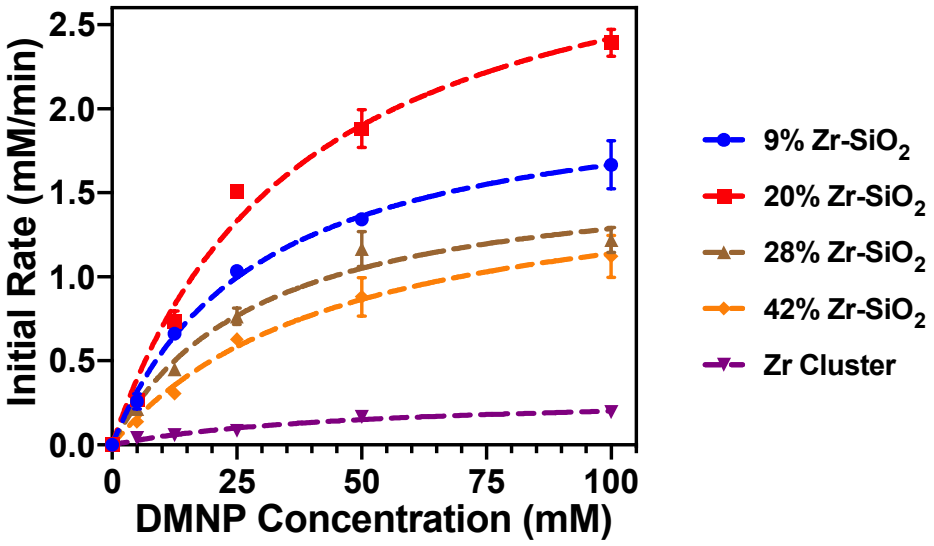

Figure 2-11 Initial rates of DMNP hydrolysis.

Table 1-2. Kinetics Results for Hydrolysis of DMNP[1]

	$t_{1/2}$[a] (min)	K_{cat}[b] $\times 10^{-2}$ (s^{-1})	K_m[c] (mM)	K_{cat}/K_m[d] ($M^{-1}s^{-1}$)
Zr_6-cluster	306 ± 9	0.21 ± 0.03	50.8 ± 9.3	0.04 ± 0.01
9% Zr-SiO_2	11.2 ± 1.1	1.53 ± 0.18	29.3 ± 6.1	0.53 ± 0.05
20% Zr-SiO_2	6.5 ± 0.3	2.36 ± 0.13	37.3 ± 2.3	0.63 ± 0.01
28% Zr-SiO_2	20.4 ± 2.1	1.18 ± 0.10	29.3 ± 4.6	0.41 ± 0.05
42% Zr-SiO_2	36.3 ± 1.6	1.19 ± 0.21	46.6 ± 9.5	0.26 ± 0.02

[1] Conditions: 2.35 mM Zr_6-cluster to DMNP in NEM buffer pH 10. [a] 9.4 mol% Zr_6-cluster to DMNP. $t_{1/2}$ was calculated by ln (2)/k, where k is the pseudo-first order rate constant (min^{-1}). [b] Turn over number (K_{cat}) is derived by the MM model with the Zr_6-cluster concentration of 2.35 mM. [c]K_m is extrapolated as the substrate concentration (mM) at one-half of the theoretical maximum initial rate (V_{max}), which is determined using the MM model. [d] Catalytic efficiency (K_{cat}/K_m).

2.6. HYDROLYSIS OF DMNP UNDER RELEVANT CONDITIONS

Hydrogel is a family of hydrophilic polymers, which are known for their flexibility and water absorbing capability. Within a series of polymeric materials, the high density of basic amine groups in polyethyleneimine (PEI) has demonstrated aiding for the catalytic decomposition of DMNP.[46, 47] To develop a hybridization of the Zr-SiO_2, bPEI hydrogel (bPEIH), and fabrics as a component of an outer garment that will prevent the contact of NAs to the wearer, a simple approach was described here to attach the catalytic NPs on bPEIH coated fabric cloth.

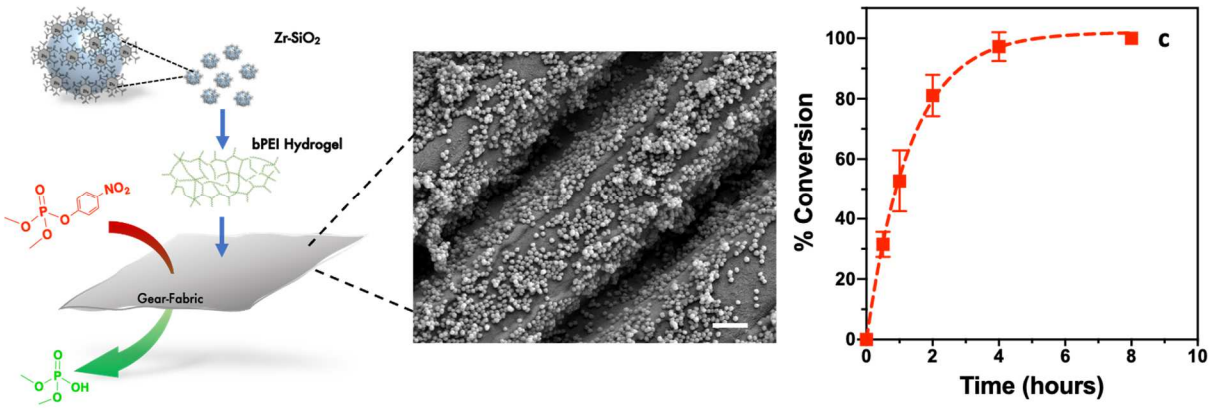

Figure 2-12 Schematic drawing of loading Zr-SiO2 NPs and bPEIH on a fabric swatch (left), SEM images of loaded fabric (middle), and hydrolysis of 25 mM DMNP at room temperature without addition of aqueous water (right).

In brief, an aqueous suspension of Zr-SiO_2 NPs was drop-casted onto a crosslinked bPEI coated fabric sheet, which is composed of Nylon and polylactic acid. The intertwined fabric has multiple microchannels (~1 μm width) in a single thread for maximizing the retention of the NPs against abrasion and laundering (data not shown here). This morphology of the fabric provides slots for hosting NPs and avoids the demand for additional functionalization. A layer-by-layer

approach described in this work minimizes the embedding of Zr^{IV} active sites into the polymeric hydrogel matrix and thus leads to a maximum exposure of the Zr-SiO_2 NPs on surface, comparing to the one-step method. To maintain the water content, the composited fabric was stored in a closed vial at room temperature at all times. The SEM image shown in Figure 2-12 (mid) revealed a dense and continuous coverage of the particles inside the microchannels. The solid-state catalytic hydrolysis of DMNP with the fabric composite demonstrated an initial half-life of 90 mins and a near quantitative conversion (97%) after 4 hours (Figure 2-12). The control experiments for the bPEIH/Fabric (9.0 ± 3.0%), Zr-SiO_2/Fabric (24.0 ± 1.2%), and the bare fabric (0 ± 0%) show significantly inferior total conversions after 8 hours (Figure 2-13), confirming that the nanocatalyst requires a base and water for a completion of the reaction. The diminished catalytic rate of the Zr-SiO_2/bPEIH/Fabric composite is presumably attributed to the low mobility of the agent under solid-state condition as well as a quantity of Zr-SiO_2 NPs buried inside the microchannels, making them not readily reactive to DMNP. Interestingly, further investigation with ^{31}P NMR spectroscopy (Figure 2-13) for the bPEIH/Fabric sample, we found a formation of a singlet at -7 ppm in addition to the known chemical shift of DMNP (-5.5 ppm) and DMP (0.3 ppm). This peak is corresponded to methyl 4-nitrophenyl phosphate (M4NP, toxic), a product of the nucleophilic attack reaction between the amines of the bPEIH and methoxy group of the DMNP.[48] However, virtually no formations of M4NP were observed for the Zr-SiO_2/bPEIH/Fabric during the time course, indicating the majority of the DMNP are rapidly accessed by the surface exposed nanocatalyst instead of the bPEIH.

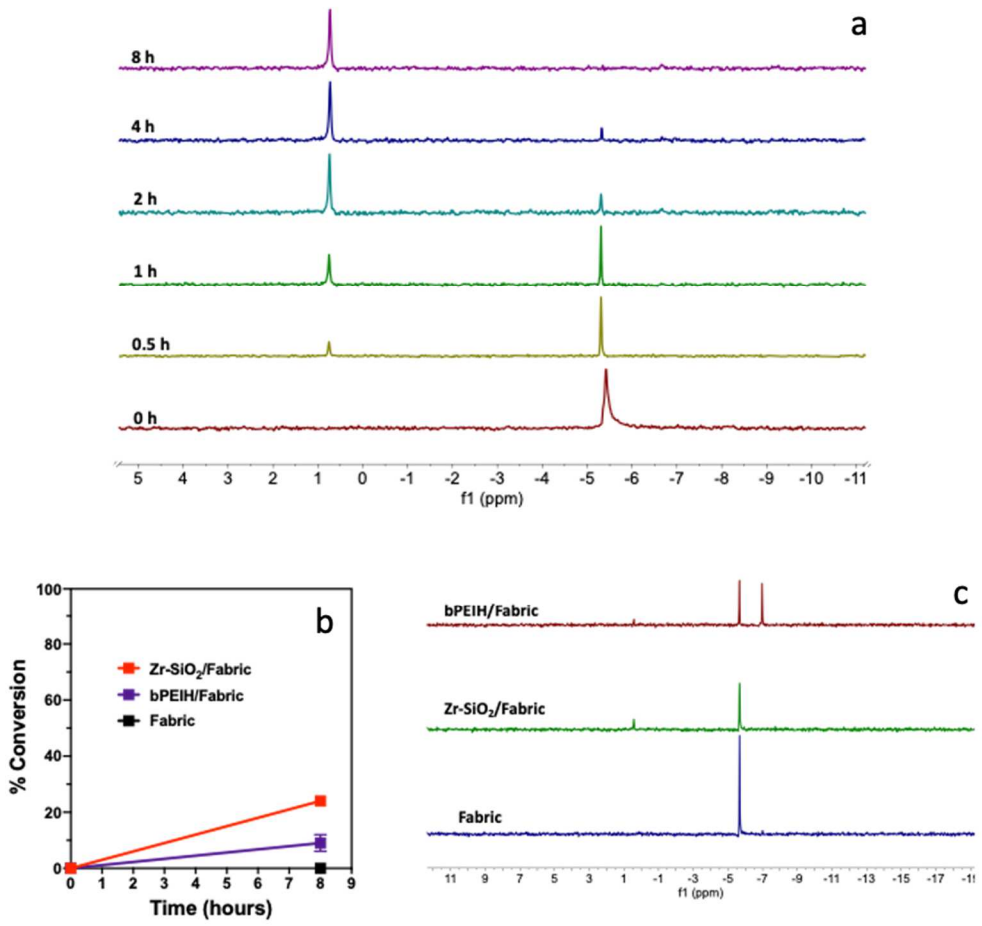

Figure 2-13 (a) ^{31}P NMR spectra following the solid state hydrolysis reaction of DMNP using Zr-SiO_2/bPEIH/Fabric composite at each time intervals. (b) Percent conversion of DMNP as a function of time, for control groups. (c) ^{31}P NMR spectra for the control groups.

2.7. CONCLUSION

UV-induced silica surface radicals promoted a highly efficient mean to conjugate Zr_6-cluster to the surface of the NP via photopolymerization under the presence of BP. In comparison to the free Zr_6-cluster, the immobilized cluster showed a remarkable enhancement of the hydrolytic half-life towards the neutralization of DMNP, attributing to the enhanced dispersity in aqueous media that enables more diffusion pathways for the substrate to the catalytic sites. Finally, a crucial step for practical use of this conjugated nanocatalyst in protective garment was rationalized. The

high density of amine in a water-based hydrogel polymer preserves an amount of imminent water under basic condition for solid-state hydrolysis of DMNP. This facile integration of Zr-SiO_2/bPEIH/Fabric demonstrated the first example of modified NPs for solid-state hydrolysis of nerve agent simulant with a promising result for the future protective wearable.

3. MESOPOROUS SILICA LOADED WITH ZIRCONIUM CLUSTER FOR AMMONIA ADSORPTION

3.1. INTRODUCTION

Ammonia (NH_3) plays an invaluable role in many industrial settings as a chemical feedstock, refrigerant gas, and most importantly as a fertilizer.[49] It is widely used, yet it is a highly toxic and corrosive gas, which causes severe damage to human eyes, the respiratory tract, and lungs even at low concentrations.[19] The NH_3 exposure limit set by the National Institute for Occupational Safety and Health (NIOSH) of the USA is 35 ppm for a short time (15 minutes).[50] Therefore, sorbents capable of removing trace NH_3 are of interest for industrial air purification, personal protective equipment, and gas isolation. For this requirement, the uptake of NH_3 at low concentration is required, yet the current industrial grade sorbents, typically activated carbon, suffered from low capacity and as well as limited affinity to NH_3.[19, 50] Among the development of new materials for NH_3 adsorption, recent efforts have focused MOFs. They are a new class of crystalline porous materials, the reticular structures in which are composed of metal ions coordinated by organic linkers via strong covalent bonds. Efforts have been devoted into varying the pore size of the reticular structures[51], changing and/or introducing new identity of Lewis acidic ions to build the cluster[52], lowering the connectivity of the Lewis acidic sites[53], and tuning the activation temperature[54] to impart higher affinity for the NH_3 molecules. However, two major

obstacles preventing some MOFs from wide-spread utilization are poor hydrothermal stability and residue of harsh organic solvents.[55] The structure and porosity of some MOFs collapse upon exposure to water and high temperature, thereby reducing their effectiveness for many practical applications. Hazardous solvents such as DMF and DMSO are frequently used during the synthesis of MOFs and have high affinity to the material, removal of which requires prolonged time and special equipment; therefore, hinder their downstream applications and pose a safety concern if not being removed properly.

Given that the Lewis acidic sites of Zr-MOFs are the Zr cluster nodes, $[Zr_6O_4(OH)_4]^{12+}$, and realizing the challenge posed by nonprocessable MOF particles, we endeavored to use zirconium (oxo) hydroxy methacrylate (Zr cluster), structural in which is $Zr_6O_4(OH)_4(MA)_{12}$, to capture NH_3 gas for the first time. However, without incorporating the Zr cluster into templates, these powdery molecules aggregated, thereby, reducing its effectiveness.[14, 16, 56] Thus, it is necessary to apply a porous template to incorporate the cluster to maximize reactivity.

To construct a new composite material for Zr cluster, a high-capacity sorbent material was selected to host the clusters. MCM41 silica is one of the most well-known mesoporous constructs that was prepared by using quaternary ammonium cationic surfactants during its formation.[57] It was developed by Mobil Cooperation and became a widespread material because the highly ordered mesopores and high internal surface area can be tailored for specific adsorption tasks, such as ammonia (NH_3).[58-60] To explore the composite effect on the MCM41, LeVan and the team have reported that impregnate active metal sites, such as $Zn^{4+/2+}$, $Cu^{2+/+}$, and $Fe^{3+/2+}$, into MCM41 can enhance two to four times of the NH_3 adsorption than the base MCM41 material, and a high NH_3 adsorption Cu-BTC (MOF) which crystalized inside the MCM41 pores retains 50% of the adsorption capacity meanwhile enhances the Cu-BTC's hydrothermal stability.[58, 59] However,

impregnated species using a physical attachment approach tends to leach out from its template material and reduces the composite's activity. To mitigate this problem, a stronger adhesion method for the impregnated species is described in this text. Zr clusters are first fully dispersed throughout the silica matrix using an impregnation technique then polymerized in the pore under UV light, the covalent grafting in which prevents small molecules (Zr cluster ca. 1.7 nm)[12] escaping from their template material.

This research focuses on toxic gas filtration for the interest of personal protective wearable used on field, so measurements of NH_3 gas breakthrough was performed at a reduced NH_3 concentration (0.01%), which is orders of magnitude more dilute than pure NH_3, and generally yields lower NH_3 capacity values for common adsorbents.[58] We characterized the Zr cluster loaded MCM-41 samples via N_2 adsorption-desorption isotherms, TGA, SEM, and finally analyzed the NH_3 breakthrough. Overall, Zr cluster incorporated MCM-41 was found to be effective at enhancing the ammonia capacity with near 3 times enhancement of the capacity of the unloaded MCM41 material.

3.2. GRAFTING OF ZR CLUSTER ON A POROUS MATERIAL

A typical synthesis of MCM-41 nanoparticles (MCM41NP) is as follow[61]: in a 500 mL flask, 0.75 g of cetyltrimethyl ammonium bromide (CTAB) was dissolved in 360 mL of water at 75˚C with fast stirring. 5.25 mL of 1 M NaOH and 4 mL of TEOS were added to the heated solution and stirred for 2 hours. The white suspension silica particles were collected by centrifugation at 8000 rpm for 5 mins and washed with copious DI water. The dried white powder was then calcinated at 550˚C furnace for 4 hours to remove the structure directing agents. Approximately 0.8 g of MCM41NP can be collected.

In a typical experiment of Zr grafting on MCM41NP (Zr-MCM41NP), 300 mg of MCM41NP was first sonicated in 20 mL of 1 M HCl solution overnight to rehydrate the surface. After the removal of the HCl solution (centrifugation 8,000 rpm, 5 mins) then wash with THF for once, the rehydrated MCM41NP and 150 mg of benzophenone (BP) were dispersed in 30 mL of tetrahydrofuran (THF) in a 50 mL round bottom flask. The container was subjected to nitrogen to degas for 30 minutes to remove oxygen (polymerization inhibitor) prior to the UV irradiation. A high-pressure mercury lamp with broad wavelength was set to irradiate the sample for 30 mins with stirring. Excess of the free BP was then removed and subsequently washed in THF solution. To reach the 30% mass loading condition, 160 mg of the Zr cluster was added to the BP-MCM41NP and suspended in 30 mL of THF solution. The mixture was bubbled with nitrogen for 30 mins, then UV irradiated for 1.5 hour. The Zr-MCM41NP was collected by centrifugation and washed with THF to remove unbonded Zr cluster. The final composite was dried in an oven at 80˚C overnight to remove residual organic solvent.

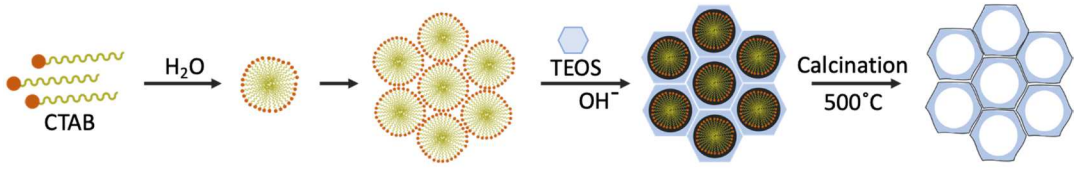

Figure 3-1 Schematic drawing of synthesis of MCM41NP.

Similar to the base-catalyzed hydrolysis-condensation for forming the Stöber silica nanoparticles, the synthesis of mesoporous silica involves an additional adding of a structure directing agent, CTAB, to regulate the internal pore structure. Figure 3-1 describes the sequential steps for the formation of mesoporous silica particles: the amphiphilic CTAB self-assemblies into cylindrical micelles in the aqueous medium, and the positively charged hydrophilic heads attract

the negatively charged silicic acid, which is the partial hydrolysis product of TEOS. Polycondensation of the silicic acid forms the silicate walls along the cylindrical micelles. The mesoporous silica particles are finally calcined at 550˚C to completely combust the structure directing agents prior to the loading experiment.

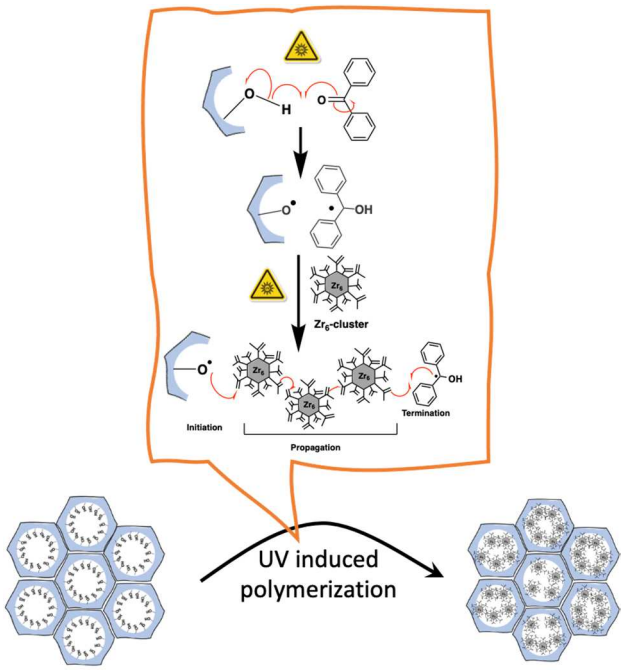

Figure 3-2 Schematic drawing of the UV induced photopolymerization of Zr cluster into MCM41NP

To immobilize the Zr cluster into the mesoporous MCM41NP, a facile UV induced polymerization protocol was adopted. The schematic drawing of the grafting mechanism was proposed in Figure 3-2. To rehydrate the MCM41NP with surface hydroxyl groups, the particles were sonicated in acidic medium (1M HCl) to rehydrate the siloxane bonds.[62, 63] The detailed discussion for the photopolymerization of Zr cluster was mentioned in the earlier chapter 2.4.

3.3. PHYSICAL CHARACTERIZATION OF ZR-MCM41NP

The SEM image and DLS measurement (Figure 3-3) confirmed the regular shapes and the uniformity of the MCM41NP, and the enlarged image revealed the surface roughness which is attributable to the mesoporous channels because no similar surface roughness was observed for the nonporous silica nanoparticles (Figure 3-3 a). DLS shows the hydrodynamic size of the Zr-MCM41NP 326.1 ± 20.0 nm (0.545 PDI), which is slightly larger than the average size of the voided MCM41NP 289.4 ± 13.2 nm (0.259 PDI). After polymerization, the particle surface was covered by the clusters, but no severe aggregation of the neighboring particles was observed. Furthermore, Figure 4-4 d. shows the Zr-MCM41NP suspension no aggregated in an alkaline medium (NEM buffer pH 10) after one hour, indicating the short-term stability of the composite material (349.0 ± 38 nm, PDI 0.525).

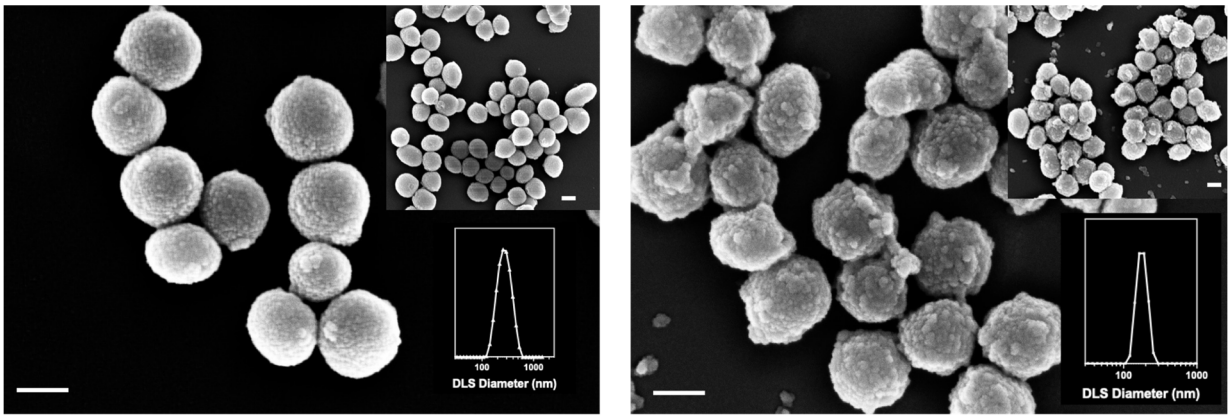

Figure 3-3 SEM images for MCM41NP and Zr-MCM41NP. Scale bars represent 100 nm.

Surface modification was further verified using FTIR. For the MCM41NP, no peak appearance near the 3000 cm^{-1} region indicates the successful removal of pore template, and a strong band at 1030 cm^{-1} associated with Si-O stretching modes of the SiO_2, and the stretching and

bending modes at 3320 cm^{-1} and 1660 cm^{-1} assigned to a combination of surface O-H and adsorbed water (Figure 3-4 b).[38, 39] Peaks appeared in the Zr-MCM41NP (Figure 3-4 b) can be identified to be the presence of the Zr clusters on the NPs. The new peaks at 1461 cm^{-1} to 1564 cm^{-1} are attributed to the asymmetric and symmetric stretching mode of the COO^-, and the stretching mode of the C-H for the methyl and olefinic group are present at 2911 cm^{-1} and 2985 cm^{-1}.

Figure 3-4 a depicts the nitrogen adsorption desorption isotherm in liquid nitrogen at -196˚C. The isotherm curves are typical of MCM41 material and is Type IV based on the IUPAC classification scheme, indicating the mesopores presence in the material. Hysteresis due to the capillary condensation in the mesopores is evident in the desorption curve, and the addition of Zr cluster does not change the mesoporosity of the material. The specific surface area was calculated by the BET theory, 664 m^2/g and 510 m^2/g for MCM41NP and Zr-MCM41NP, respectively, and the pore volumes were measure by BJH adsorption cumulative volume of pores between 1.5 nm to 100 nm, 0.29 cm^3/g and 0.24 cm^3/g for the MCM41NP and Zr-MCM41NP, respectively.

To determine the mass of the Zr cluster grafted on MCM41NP, the samples were first subjected to drying at 150˚C for 30 mins to remove entrapped solvent then to analyze the weight loss from 100˚C to 1300˚C using TGA under nitrogen flow (Figure 4-4 c). The 20% weight loss for the Zr-MCM41NP was converted to be 30% of the mass loading, following the eq 1.

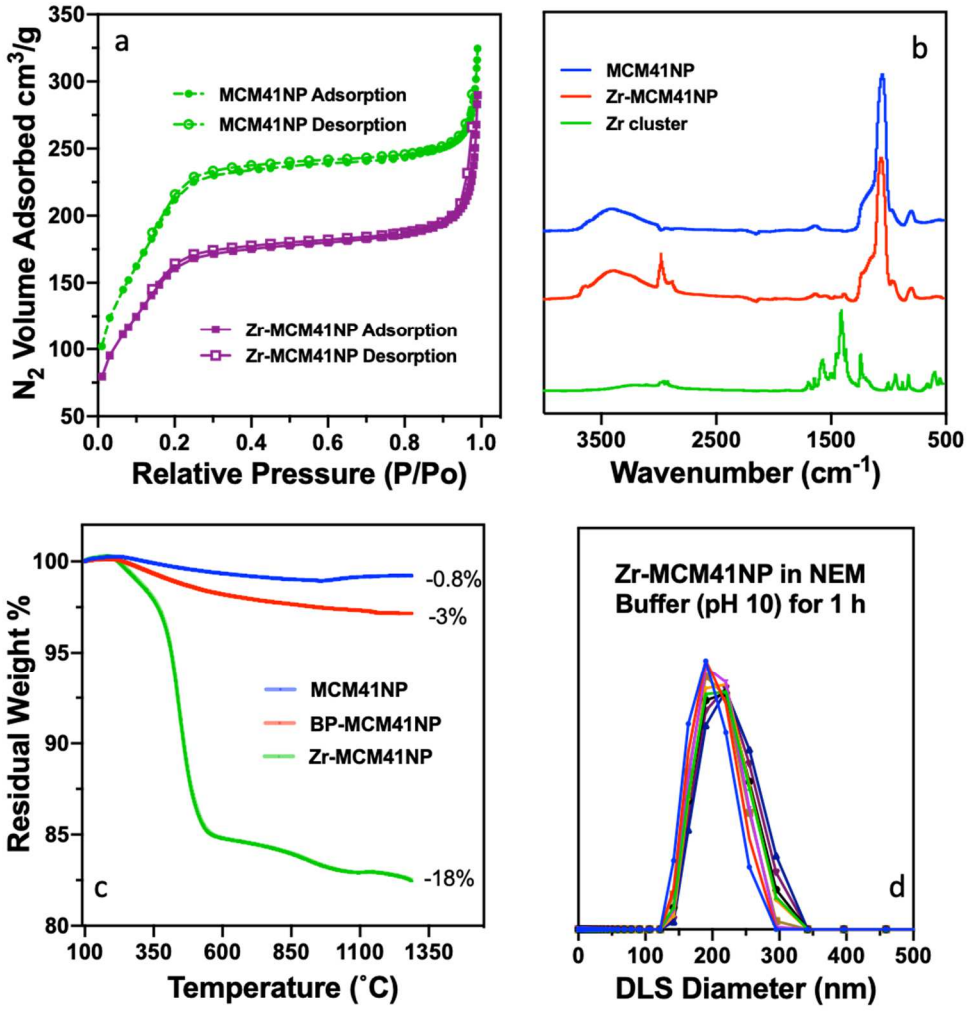

Figure 3-4 Nitrogen adsorption desorption isotherm (a). FTIR spectra (b). TGA (c). DLS size measurement (d).

3.4. PREPARATION OF AMMONIA GAS BREAKTHROUGH TEST

Before attached the particles onto the microchannel fabric, the particles had been sonicated in DI water overnight until the suspension is homogeneous. 80 µL of the particles in DI water (0.25 mg/µL) was drop-casted on the fabric (1.7 cm^2) and gently smoothened using the flat bottom of a spatula. The composited fabric was then dried in oven at 80˚C for 18 hours. The mass of an empty fabric was about 10.64 ± 0.2 mg/cm^2. The mass of the particles loaded on a fabric was 7.35 ± 0.8 mg/cm^2 and 8.29 ± 1.0 mg/cm^2 for MCM41NP and Zr-MCM41NP, respectively. The

differences of mass loading on the fabric can be attributed to the higher density of the Zr-MCM41NP, that is theoretically, 30% heavier than the empty particles.

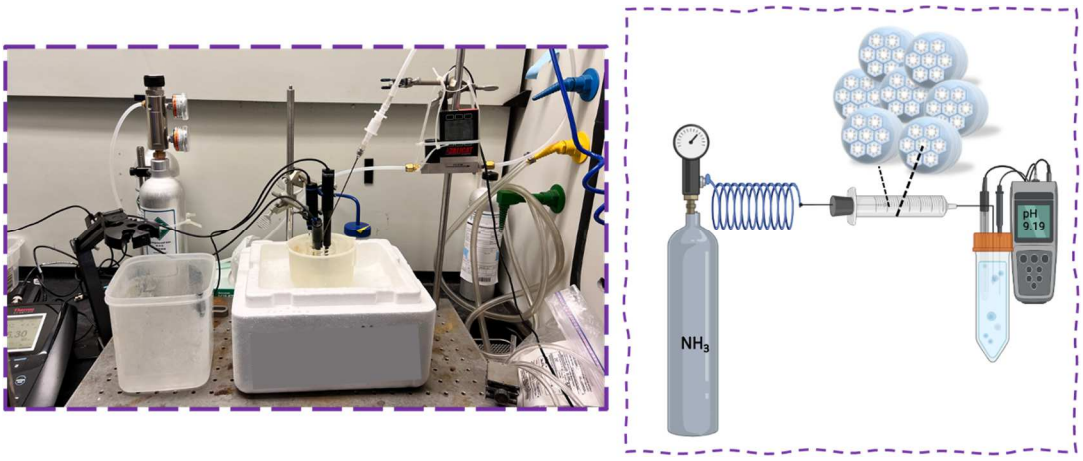

Figure 3-5 The setup for measuring the breakthrough of ammonia gas. Flow rate of the 100 ppm (0.01% in N_2) NH_3 is 100 ml/min. The sorbent material is fixated inside the sealed chamber, which has 0.28 cm^2 surface area for the breakthrough. The DI-water (30 mL) is maintained at 0˚C for pH measurement.

A qualitative study of the ammonia gas adsorption by MCM41NP and Zr-MCM41NP is reported in this paper using an indirect measurement to provide a preliminarily insight into the absorption capacity by the mesoporous materials. It is well known that ammonia (K_b 1.8×10^{-5}) is highly soluble in water and rapidly associate to form ammonia (NH_4^+) and hydroxide (OH^-) ions, which results in an increase of the pH in water. The gas molecules can penetrate the sorbent and react with its surface via different molecular interactions, and finally the effluent NH_3 can be collected in the water for the pH measurement. If the increase of the pH is delayed, it indicates that the ammonia molecules are adsorbed. To this extend, the setup of the experiment is shown in Figure 4-5. The flow rate of the ammonia gas (100 ppm in N_2) was set to 100 mL/min, and the pH

of the DI-water (initial pH 5.8, 30 mL at 0˚C) was recorded every 10 seconds using the Orion Star™ A211 Benchtop pH Meter equipped with a thermometer and a stir function.

3.5. AMMONIA GAS BREAKTHROUGH RESULTS AND DISCUSSION

Acidic molecules were expected to play an important role in the sorption capacity for ammonia because they can participate in an acid-base reaction. To validate this expectation, Zr cluster was agitated in a NaOH solution (0.1 M) for 18 hours and centrifuged to remove the solution, and the insoluble substance was subjected to FTIR. It is evident that the peak intensity of the base treated sample diminished (Figure 4-6), suggesting the self-dissociation of the Zr cluster in a basic environment. This result can be attributed to the organic backbones leaching, and the insoluble substance can be attributed to the formation of zirconium oxide/hydroxide.[64]

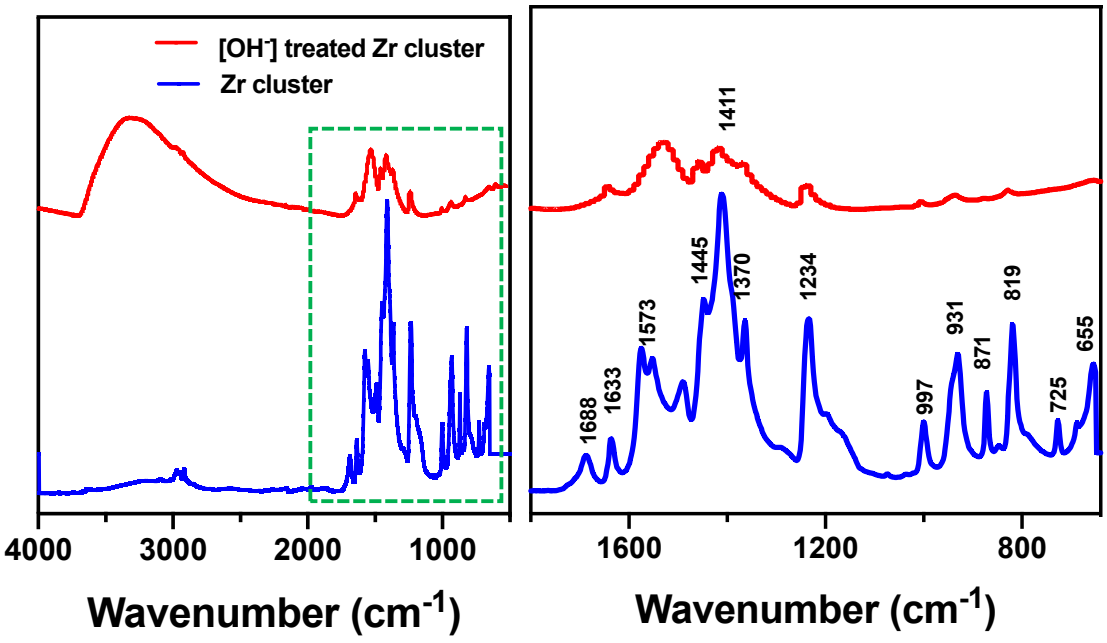

Figure 3-6 FTIR spectra for post alkaline treated Zr cluster and pristine cluster.

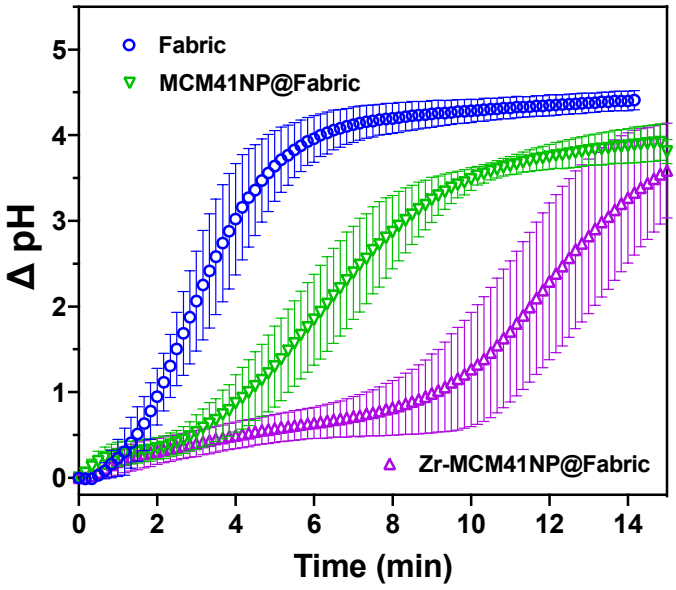

Figure 3-7 Breakthrough of ammonia gas was measured by the increase of pH in the DI-water. The active surface area for the gas breakthrough test is 0.28 cm^2 and a sorbent loading of 7.35 mg/cm^2 and 8.29 mg/cm^2 for the MCM41NP@Fabric and Zr-MCM41NP@Fabric, respectively.

In order to minimize the leakage of gas passing through the gaps between the fabric, a saturated amount of the nanoparticles was needed to cover the fabric uniformly. The result of the breakthrough test is shown in Figure 3-7, the fabric material provided a minimum amount of adsorption towards NH_3, showing a rapid breakthrough after 2.06 ± 0.41 minutes, where the breakthrough point was defined as the time required to increase the pH by one. After incorporating the MCM41NP onto the fabric material, a delayed breakthrough of the ammonia gas was evident and shows the gas breakthrough after 4.43 ± 0.93 minutes. The internal surface area of the MCM41NP provides additional sorption capacity for the NH_3. Specifically, the sonication process before the loading induced hydrolysis of the siloxane bonds on the silicate surface and endows a higher coverage of hydroxyl group (5 $\mu mol/m^2$) after rehydration[63], the hydroxyl groups which are assumed to facilitate the sorption of NH_3 gas via formation of the hydrogen bonding.[60, 65] To

estimate the sorption capacity of the sorbent material, the gas flow rate (100 mL/min), ammonia concentration (100 ppm or 0.01%), the breakthrough time, and the mass of the particles were taken into consideration. There is less than 1.62 μmol of NH_3 adsorbed by the MCM41NP before its breakthrough, and the sorption capacity is approximated 0.78 mmol NH_3 g^{-1} sorbent. A delayed breakthrough (9.62 ± 2.06 mins) of the NH_3 gas was observed for the Zr-MCM41NP. Less than 7.13 μmol of NH_3 was adsorbed by the Zr-MCM41NP and is equivalent to 2.22 mmol of NH_3 g^{-1} sorbent. The mesopores within the Zr-MCM41NP are designed to form a reservoir for storage of water, in which the ammonia gas creates a local alkaline environment in the pores and accelerates the dissociation of the cluster, that is a neutralization effect. The Brøsted acid sites (μ_3-OH) in the cluster core are attributable to the chemisorption of NH_3, and the Zr (IV) Lewis acidic active sites are responsible for the gas uptake upon NH_3 coordination.[54, 66]

Table 2-1. Summary of Zr-MCM41NP.

Material	BET Surface Area (m^2/g)	DLS size (nm)	Breakthrough Point (min)[a]	Estimated NH_3 Adsorption (mmol/g)
MCM41NP	664	289.5 ± 13.2	4.43 ± 0.93	0.79 ± 0.30
Zr-MCM41NP	510	326.1 ± 20.0	9.62 ± 2.06	2.22 ± 0.60

[a]Breakthrough is defined as the duration for pH increased by 1.

3.6. CONCLUSIONS

A novel composite material was synthesized and characterized by combining an ordered mesoporous silica nanoparticle with zirconium (oxo) hydroxy methacrylate via covalent grafting. The nitrogen isotherms confirm the mesoporous structure of the silica NP remained after grafting, and the presence of the cluster was detected by FTIR and was quantified by TGA. A practical application of the composite material was described, NPs in which were embedded in a fabric

swatch and tested for its isolation of NH_3 from N_2, and the breakthrough tests showed a delay of the gas breakthrough using bare MCM41NP, and Zr cluster loaded NP further delay the breakthrough point compared to the voided MCM41NP (4 min vs 10 min). This pilot study concluded that it is possible to utilize Zr cluster to place a specific functionality into the pores to adsorb NH_3. Although the delays of the pH raise had been concluded as the gas adsorbed by the material, a more quantitative method for calculating ammonia adsorption capacity is in demand. The future work includes using chemisorption/physisorption instrument to obtain ammonia gas adsorption-desorption isotherms for more accurately quantification of the gas adsorbed.

Acknowledgements

This material is based upon work supported by the Defense Advanced Research Agency (DARPA) and Naval Information Warfare Center Pacific, (NIWC Pacific) under Contract No. N66001-21-C-4010. Additional support received from NSF through the UC San Diego Materials Research Science and Engineering Center (UCSD MRSEC) DMR-2011924. The authors acknowledge the use of facilities and instrumentation supported by NSF through the UC San Diego Materials Research Science and Engineering Center (UCSD MRSEC) DMR-2011924. The SEM work was performed in part at the San Diego Nanotechnology Infrastructure (SDNI) of UCSD, a member of the National Nanotechnology Coordinated Infrastructure, which is supported by the National Science Foundation (Grant ECCS-2025752).

REFERENCES

(1) Kickelbick, G.; Schubert, U. Oxozirconium Methacrylate Clusters: Zr6(OH)4O4(OMc)12 and Zr4O2(OMc)12 (OMc = Methacrylate). *Chemische Berichte* **1997**, *130* (4), 473-478. DOI: 10.1002/cber.19971300406.

(2) Kickelbick, G.; Feth, M. P.; Bertagnolli, H.; Morani, B.; Trimmel, G.; Schubert, U. EXAFS Investigations on Nanocomposites Composed of Surface-Modified Zirconium and Zirconium/Titanium Mixed Metal Oxo Clusters and Organic Polymers. In *Nanostructured Materials*, Hofmann, H., Rahman, Z., Schubert, U. Eds.; Springer Vienna, 2002; pp 183-193.

(3) Kreutzer, J.; Puchberger, M.; Artner, C.; Schubert, U. Retention of the Cluster Core Structure during Ligand Exchange Reactions of Carboxylato-Substituted Metal Oxo Clusters. *European Journal of Inorganic Chemistry* **2015**, *2015* (12), 2145-2151. DOI: 10.1002/ejic.201403209.

(4) Zhang, Y.; de Azambuja, F.; Parac-Vogt, T. N. The forgotten chemistry of group(IV) metals: A survey on the synthesis, structure, and properties of discrete Zr(IV), Hf(IV), and Ti(IV) oxo clusters. *Coordination Chemistry Reviews* **2021**, *438*, 213886. DOI: 10.1016/j.ccr.2021.213886.

(5) Kickelbick, G.; Holzinger, D.; Brick, C.; Trimmel, G.; Moons, E. Hybrid Inorganic−Organic Core−Shell Nanoparticles from Surface-Functionalized Titanium, Zirconium, and Vanadium Oxo Clusters. *Chemistry of Materials* **2002**, *14* (10), 4382-4389. DOI: 10.1021/cm021216y.

(6) Girardi, F.; Fambri, L.; Maggini, S.; Di Maggio, R. Inorganic–organic hybrid materials prepared from zirconium oxo-clusters and 2-hydroxyethyl methacrylate. *Journal of Applied Polymer Science* **2015**, *132* (9). DOI: 10.1002/app.41568.

(7) Kogler, F. R.; Koch, T.; Peterlik, H.; Seidler, S.; Schubert, U. Mechanical, thermomechanical, and thermal properties of polystyrene crosslinked with a multifunctional zirconium oxo cluster.

Journal of Polymer Science Part B: Polymer Physics **2007**, *45* (16), 2215-2231. DOI: 10.1002/polb.21224.

(8) Kickelbick, G.; Feth, M. P.; Bertagnolli, H.; Morani, B.; Trimmel, G.; Schubert, U. EXAFS Investigations on Nanocomposites Composed of Surface-Modified Zirconium and Zirconium/Titanium Mixed Metal Oxo Clusters and Organic Polymers. *Nanostructured Materials* **2002**, 183-193. DOI: 10.1007/978-3-7091-6740-3_16.

(9) Guillerm, V.; Gross, S.; Serre, C.; Devic, T.; Bauer, M.; Férey, G. A zirconium methacrylate oxocluster as precursor for the low-temperature synthesis of porous zirconium(iv) dicarboxylates. *Chemical Communications* **2010**, *46* (5), 767-769, 10.1039/B914919H. DOI: 10.1039/B914919H.

(10) Bezrukov, A. A.; Törnroos, K. W.; Le Roux, E.; Dietzel, P. D. C. Incorporation of an intact dimeric Zr12 oxo cluster from a molecular precursor in a new zirconium metal–organic framework. *Chemical Communications* **2018**, *54* (22), 2735-2738, 10.1039/C8CC00507A. DOI: 10.1039/C8CC00507A.

(11) Oliveira, D. C.; Macedo, A. G.; Silva, N. J. O.; Molina, C.; Ferreira, R. A. S.; André, P. S.; Dahmouche, K.; Bermudez, V. D. Z.; Messaddeq, Y.; Ribeiro, S. J. L.; et al. Photopatternable Di-ureasil−Zirconium Oxocluster Organic−Inorganic Hybrids As Cost Effective Integrated Optical Substrates. *Chemistry of Materials* **2008**, *20* (11), 3696-3705. DOI: 10.1021/cm7031702.

(12) Kataoka, S.; Sue, K. Enhanced Solubility of Zirconium Oxo Clusters from Diacetoxyzirconium(IV) Oxide Aqueous Solution as Inorganic Extreme-Ultraviolet Photoresists. *European Journal of Inorganic Chemistry* **2022**, *2022* (12), e202200050. DOI: 10.1002/ejic.202200050.

(13) Soares, B. G.; Caplan, S.; Livi, S.; Gatti, A.; Ribeiro, S. J. L. Zirconium-methacrylate oxoclusters as new hybrid materials for the modification of epoxy systems. *J. Mater. Sci.* **2015**, *50* (7), 2903-2913. DOI: 10.1007/s10853-015-8854-y.

(14) Faccioli, F.; Bauer, M.; Pedron, D.; Sorarù, A.; Carraro, M.; Gross, S. Hydrolytic Stability and Hydrogen Peroxide Activation of Zirconium-Based Oxoclusters. *European Journal of Inorganic Chemistry* **2015**, *2015* (2), 210-225. DOI: 10.1002/ejic.201402767.

(15) Ma, L.; Xie, J.; Yan, X.; Fan, Z.; Li, H.; Lu, L.; Chen, L.; Xin, Y.; Yin, P. Wearable membranes from zirconium-oxo clusters cross-linked polymer networks for ultrafast chemical warfare agents decontamination. *Chinese Chemical Letters* **2021**. DOI: 10.1016/j.cclet.2021.10.059.

(16) Su, S.; Jung, D.; Gong, X.; Idrees, K. B.; Hanna, S. L.; Islamoglu, T.; Gianneschi, N. C.; Farha, O. K. Aggregation-Suppressed Porous Processable Hexa-Zirconium/Polymer Composites for Detoxification of a Nerve Agent Simulant. *Chemistry of Materials* **2022**, *34* (11), 4983-4991. DOI: 10.1021/acs.chemmater.2c00262.

(17) Cubicciotti, D. The Melting Point—Composition Diagram of the Zirconium—Oxygen System1. *J. Am. Chem. Soc.* **1951**, *73* (5), 2032-2035. DOI: 10.1021/ja01149a038.

(18) Raushel, F. M. Catalytic detoxification. *Nature* **2011**, *469* (7330), 310-311. DOI: 10.1038/469310a.

(19) DeCoste, J. B.; Peterson, G. W. Metal–Organic Frameworks for Air Purification of Toxic Chemicals. *Chemical Reviews* **2014**, *114* (11), 5695-5727. DOI: 10.1021/cr4006473.

(20) Barton, H. F.; Jamir, J. D.; Davis, A. K.; Peterson, G. W.; Parsons, G. N. Doubly Protective MOF-Photo-Fabrics: Facile Template-Free Synthesis of PCN-222-Textiles Enables Rapid Hydrolysis, Photo-Hydrolysis and Selective Oxidation of Multiple Chemical Warfare Agents and Simulants. *Chemistry – A European Journal* **2021**, *27* (4), 1465-1472. DOI: 10.1002/chem.202003716.

(21) Robert W, M. NBC FILTER PERFORMANCE. Defense Technical Information Center: Edgewood Chemical Biological Center, 2001.

(22) Jung, D.; Das, P.; Atilgan, A.; Li, P.; Hupp, J. T.; Islamoglu, T.; Kalow, J. A.; Farha, O. K. Reactive Porous Polymers for Detoxification of a Chemical Warfare Agent Simulant. *Chemistry of Materials* **2020**, *32* (21), 9299-9306. DOI: 10.1021/acs.chemmater.0c03160.

(23) Jung, D.; Kirlikovali, K. O.; Chen, Z.; Idrees, K. B.; Atilgan, A.; Cao, R.; Islamoglu, T.; Farha, O. K. An Amidoxime-Functionalized Porous Reactive Fiber against Toxic Chemicals. *ACS Materials Letters* **2021**, *3* (4), 320-326. DOI: 10.1021/acsmaterialslett.0c00598.

(24) Kwon, W.; Kim, C.; Kim, J.; Kim, J.; Jeong, E. Facile Fabric Detoxification Treatment Method Using Microwave and Polyethyleneimine Against Nerve Gas Agents. *Polymers* **2020**, *12* (12). DOI: 10.3390/polym12122861.

(25) Lyu, Y.; Morillas-Becerril, L.; Mancin, F.; Scrimin, P. Hydrolytic cleavage of nerve agent simulants by gold nanozymes. *Journal of Hazardous Materials* **2021**, *415*, 125644. DOI: 10.1016/j.jhazmat.2021.125644.

(26) Bromberg, L.; Hatton, T. A. Nerve Agent Destruction by Recyclable Catalytic Magnetic Nanoparticles. *Ind. Eng. Chem. Res.* **2005**, *44* (21), 7991-7998. DOI: 10.1021/ie0506926.

(27) Kirlikovali, K. O.; Chen, Z.; Islamoglu, T.; Hupp, J. T.; Farha, O. K. Zirconium-Based Metal–Organic Frameworks for the Catalytic Hydrolysis of Organophosphorus Nerve Agents. *ACS Appl. Mater.* **2020**, *12* (13), 14702-14720. DOI: 10.1021/acsami.9b20154.

(28) Katz, M. J.; Mondloch, J. E.; Totten, R. K.; Park, J. K.; Nguyen, S. T.; Farha, O. K.; Hupp, J. T. Simple and compelling biomimetic metal-organic framework catalyst for the degradation of nerve agent simulants. *Angew Chem Int Ed Engl* **2014**, *53* (2), 497-501. DOI: 10.1002/anie.201307520.

(29) Mondloch, J. E.; Katz, M. J.; Isley Iii, W. C.; Ghosh, P.; Liao, P.; Bury, W.; Wagner, G. W.; Hall, M. G.; DeCoste, J. B.; Peterson, G. W.; et al. Destruction of chemical warfare agents using metal–organic frameworks. *Nat. Mater.* **2015**, *14* (5), 512-516. DOI: 10.1038/nmat4238.

(30) Moon, S.-Y.; Liu, Y.; Hupp, J. T.; Farha, O. K. Instantaneous Hydrolysis of Nerve-Agent Simulants with a Six-Connected Zirconium-Based Metal–Organic Framework. *Angewandte Chemie International Edition* **2015**, *54* (23), 6795-6799. DOI: 10.1002/anie.201502155.

(31) Katz, M. J.; Moon, S.-Y.; Mondloch, J. E.; Beyzavi, M. H.; Stephenson, C. J.; Hupp, J. T.; Farha, O. K. Exploiting parameter space in MOFs: a 20-fold enhancement of phosphate-ester hydrolysis with UiO-66-NH2. *Chem. Sci.* **2015**, *6* (4), 2286-2291, 10.1039/C4SC03613A. DOI: 10.1039/C4SC03613A.

(32) Palomba, J. M.; Credille, C. V.; Kalaj, M.; DeCoste, J. B.; Peterson, G. W.; Tovar, T. M.; Cohen, S. M. High-throughput screening of solid-state catalysts for nerve agent degradation. *ChemComm* **2018**, *54* (45), 5768-5771. DOI: 10.1039/C8CC03255F.

(33) Sandhu, S. S.; Kotagiri, Y. G.; Fernando I, P. U. A. I.; Kalaj, M.; Tostado, N.; Teymourian, H.; Alberts, E. M.; Thornell, T. L.; Jenness, G. R.; Harvey, S. P.; et al. Green MIP-202(Zr) Catalyst: Degradation and Thermally Robust Biomimetic Sensing of Nerve Agents. *J. AM. Chem. Soc.* **2021**, *143* (43), 18261-18271. DOI: 10.1021/jacs.1c08356.

(34) Croissant, J. G.; Butler, K. S.; Zink, J. I.; Brinker, C. J. Synthetic amorphous silica nanoparticles: toxicity, biomedical and environmental implications. *Nat. Rev. Mater.* **2020**, *5* (12), 886-909. DOI: 10.1038/s41578-020-0230-0.

(35) Stöber, W.; Fink, A.; Bohn, E. Controlled growth of monodisperse silica spheres in the micron size range. *Journal of Colloid and Interface Science* **1968**, *26* (1), 62-69. DOI: 10.1016/0021-9797(68)90272-5.

(36) Gao, W.; Rigout, M.; Owens, H. Facile control of silica nanoparticles using a novel solvent varying method for the fabrication of artificial opal photonic crystals. *J Nanopart Res* **2016**, *18* (12), 387. DOI: 10.1007/s11051-016-3691-8.

(37) Zhuravlev, L. T. Concentration of hydroxyl groups on the surface of amorphous silicas. *Langmuir* **1987**, *3* (3), 316-318. DOI: 10.1021/la00075a004.

(38) Khoonsap, S.; Narkkun, T.; Ratphonsan, P.; Klinsrisuk, S.; Amnuaypanich, S. Enhancing the grafting of poly(2-hydroxyethyl methacrylate) on silica nanoparticles (SiO2-g-PHEMA) by the sequential UV-induced graft polymerization with a multiple-UV irradiation. *Advanced Powder Technology* **2014**, *25* (4), 1304-1310. DOI: 10.1016/j.apt.2014.03.010.

(39) Kim, S.; Kim, E.; Kim, S.; Kim, W. Surface modification of silica nanoparticles by UV-induced graft polymerization of methyl methacrylate. *J Colloid Interface Sci* **2005**, *292* (1), 93-98. DOI: 10.1016/j.jcis.2005.09.046.

(40) Ma, H.; Davis, R. H.; Bowman, C. N. A Novel Sequential Photoinduced Living Graft Polymerization. *Macromolecules* **2000**, *33* (2), 331-335. DOI: 10.1021/ma990821s.

(41) Wang, J.; Kumeria, T.; Bezem, M. T.; Wang, J.; Sailor, M. J. Self-Reporting Photoluminescent Porous Silicon Microparticles for Drug Delivery. *ACS Applied Materials & Interfaces* **2018**, *10* (4), 3200-3209. DOI: 10.1021/acsami.7b09071.

(42) Delmas, T.; Fraichard, A.; Bayle, P.-A.; Texier, I.; Bardet, M.; Baudry, J.; Bibette, J.; Couffin, A.-C. Encapsulation and Release Behavior from Lipid Nanoparticles: Model Study with Nile Red Fluorophore. *J. Colloid Sci. Biotechnol* **2012**, *1*, 16-25. DOI: 10.1166/jcsb.2012.1010.

(43) Yang, W.; Rånby, B. Radical Living Graft Polymerization on the Surface of Polymeric Materials. *Macromolecules* **1996**, *29* (9), 3308-3310. DOI: 10.1021/ma9515543.

(44) Breger, J. C.; Ancona, M. G.; Walper, S. A.; Oh, E.; Susumu, K.; Stewart, M. H.; Deschamps, J. R.; Medintz, I. L. Understanding How Nanoparticle Attachment Enhances Phosphotriesterase Kinetic Efficiency. *ACS Nano* **2015**, *9* (8), 8491-8503. DOI: 10.1021/acsnano.5b03459.

(45) Gabrielli, L.; Prins, L. J.; Rastrelli, F.; Mancin, F.; Scrimin, P. Hydrolytic Nanozymes. *European Journal of Organic Chemistry* **2020**, *2020* (32), 5044-5055. DOI: 10.1002/ejoc.202000356.

(46) Chen, Z.; Ma, K.; Mahle, J. J.; Wang, H.; Syed, Z. H.; Atilgan, A.; Chen, Y.; Xin, J. H.; Islamoglu, T.; Peterson, G. W.; et al. Integration of Metal-Organic Frameworks on Protective Layers for Destruction of Nerve Agents under Relevant Conditions. *J Am Chem Soc* **2019**, *141* (51), 20016-20021. DOI: 10.1021/jacs.9b11172.

(47) Ma, K.; Wasson, M. C.; Wang, X.; Zhang, X.; Idrees, K. B.; Chen, Z.; Wu, Y.; Lee, S.-J.; Cao, R.; Chen, Y.; et al. Near-instantaneous catalytic hydrolysis of organophosphorus nerve agents with zirconium-based MOF/hydrogel composites. *Chem Catalysis* **2021**, *1* (3), 721-733. DOI: 10.1016/j.checat.2021.06.008.

(48) Wang, H.; Mahle, J. J.; Tovar, T. M.; Peterson, G. W.; Hall, M. G.; DeCoste, J. B.; Buchanan, J. H.; Karwacki, C. J. Solid-Phase Detoxification of Chemical Warfare Agents using Zirconium-Based Metal Organic Frameworks and the Moisture Effects: Analyze via Digestion. *ACS Appl Mater Interfaces* **2019**, *11* (23), 21109-21116. DOI: 10.1021/acsami.9b04927.

(49) Zhang, X.; Davidson, E. A.; Mauzerall, D. L.; Searchinger, T. D.; Dumas, P.; Shen, Y. Managing nitrogen for sustainable development. *Nature* **2015**, *528* (7580), 51-59. DOI: 10.1038/nature15743.

(50) Britt, D.; Tranchemontagne, D.; Yaghi, O. M. Metal-organic frameworks with high capacity and selectivity for harmful gases. *Proceedings of the National Academy of Sciences* **2008**, *105* (33), 11623-11627. DOI: 10.1073/pnas.0804900105 (acccessed 2022/08/31).

(51) Rieth, A. J.; Dincă, M. Controlled Gas Uptake in Metal–Organic Frameworks with Record Ammonia Sorption. *Journal of the American Chemical Society* **2018**, *140* (9), 3461-3466. DOI: 10.1021/jacs.8b00313.

(52) Kirlikovali, K. O.; Chen, Z.; Wang, X.; Mian, M. R.; Alayoglu, S.; Islamoglu, T.; Farha, O. K. Investigating the Influence of Hexanuclear Clusters in Isostructural Metal–Organic Frameworks on Toxic Gas Adsorption. *ACS Applied Materials & Interfaces* **2022**, *14* (2), 3048-3056. DOI: 10.1021/acsami.1c20518.

(53) Chen, Y.; Zhang, X.; Ma, K.; Chen, Z.; Wang, X.; Knapp, J.; Alayoglu, S.; Wang, F.; Xia, Q.; Li, Z.; et al. Zirconium-Based Metal–Organic Framework with 9-Connected Nodes for Ammonia Capture. *ACS Applied Nano Materials* **2019**, *2* (10), 6098-6102. DOI: 10.1021/acsanm.9b01534.

(54) Liu, J.; Lu, Z.; Chen, Z.; Rimoldi, M.; Howarth, A. J.; Chen, H.; Alayoglu, S.; Snurr, R. Q.; Farha, O. K.; Hupp, J. T. Ammonia Capture within Zirconium Metal–Organic Frameworks: Reversible and Irreversible Uptake. *ACS Applied Materials & Interfaces* **2021**, *13* (17), 20081-20093. DOI: 10.1021/acsami.1c02370.

(55) Zhang, X.; Chen, Z.; Liu, X.; Hanna, S. L.; Wang, X.; Taheri-Ledari, R.; Maleki, A.; Li, P.; Farha, O. K. A historical overview of the activation and porosity of metal–organic frameworks. *Chemical Society Reviews* **2020**, *49* (20), 7406-7427, 10.1039/D0CS00997K. DOI: 10.1039/D0CS00997K.

(56) Ma, L.; Xie, J.; Yan, X.; Fan, Z.; Li, H.; Lu, L.; Chen, L.; Xin, Y.; Yin, P. Wearable membranes from zirconium-oxo clusters cross-linked polymer networks for ultrafast chemical warfare agents decontamination. *Chinese Chemical Letters* **2022**, *33* (6), 3241-3244. DOI: https://doi.org/10.1016/j.cclet.2021.10.059.

(57) Kresge, C. T.; Leonowicz, M. E.; Roth, W. J.; Vartuli, J. C.; Beck, J. S. Ordered mesoporous molecular sieves synthesized by a liquid-crystal template mechanism. *Nature* **1992**, *359* (6397), 710-712. DOI: 10.1038/359710a0.

(58) Furtado, A. M. B.; Liu, J.; Wang, Y.; LeVan, M. D. Mesoporous silica–metal organic composite: synthesis, characterization, and ammonia adsorption. *Journal of Materials Chemistry* **2011**, *21* (18), 6698-6706, 10.1039/C1JM10451A. DOI: 10.1039/C1JM10451A.

(59) Furtado, A. M. B.; Wang, Y.; Glover, T. G.; LeVan, M. D. MCM-41 impregnated with active metal sites: Synthesis, characterization, and ammonia adsorption. *Microporous and Mesoporous Materials* **2011**, *142* (2), 730-739. DOI: 10.1016/j.micromeso.2011.01.027.

(60) Ruckart, K. N.; Zhang, Y.; Reichert, W. M.; Peterson, G. W.; Glover, T. G. Sorption of Ammonia in Mesoporous-Silica Ionic Liquid Composites. *Industrial & Engineering Chemistry Research* **2016**, *55* (47), 12191-12204. DOI: 10.1021/acs.iecr.6b02041.

(61) Yang, Y.; Song, W.; Wang, A.; Zhu, P.; Fei, J.; Li, J. Lipid coated mesoporous silica nanoparticles as photosensitive drug carriers. *Phys Chem Chem Phys* **2010**, *12* (17), 4418-4422. DOI: 10.1039/b924370d From NLM Medline.

(62) Cypryk, M.; Apeloig, Y. Mechanism of the Acid-Catalyzed Si−O Bond Cleavage in Siloxanes and Siloxanols. A Theoretical Study. *Organometallics* **2002**, *21* (11), 2165-2175. DOI: 10.1021/om011055s.

(63) Kumar, D.; Schumacher, K.; du Fresne von Hohenesche, C.; Grün, M.; Unger, K. K. MCM-41, MCM-48 and related mesoporous adsorbents: their synthesis and characterisation. *Colloids and Surfaces A: Physicochemical and Engineering Aspects* **2001**, *187-188*, 109-116. DOI: 10.1016/S0927-7757(01)00638-0.

(64) Yuan, S.; Peng, J.; Zhang, Y.; Shao-Horn, Y. Stability Trend of Metal–Organic Frameworks with Heterometal-Modified Hexanuclear Zr Building Units. *The Journal of Physical Chemistry C* **2019**, *123* (46), 28266-28274. DOI: 10.1021/acs.jpcc.9b08749.

(65) Blomfield, G. A.; Little, L. H. Chemisorption of Ammonia on Silica. *Canadian Journal of Chemistry* **1973**, *51* (11), 1771-1781. DOI: 10.1139/v73-265 (acccessed 2022/08/29).

(66) Liu, J.; Chen, Z.; Wang, R.; Alayoglu, S.; Islamoglu, T.; Lee, S.-J.; Sheridan, T. R.; Chen, H.; Snurr, R. Q.; Farha, O. K.; et al. Zirconium Metal–Organic Frameworks Integrating Chloride Ions for Ammonia Capture and/or Chemical Separation. *ACS Applied Materials & Interfaces* **2021**, *13* (19), 22485-22494. DOI: 10.1021/acsami.1c03717.